OPTIC NERVE SUBARACHNOID SPACE CEREBRAL SPINAL FLUID

COMPUTATIONAL FLUID DYNAMICS

A THESIS IN
Mechanical Engineering

Presented to the Faculty of the University
of Missouri-Kansas City in partial fulfillment of
the requirements for the degree
MASTER OF SCIENCE

By:
VINCENT LEVI RYAN KENT

B.S.M.E, University of Missouri-Kansas City, 2020

Kansas City, Missouri
2021

OPTIC NERVE SUBARACHNOID SPACE CEREBRAL SPINAL FLUID COMPUTATIONAL FLUID DYNAMICS

Vincent Levi Ryan Kent, Candidate for the Master of Science Degree

University of Missouri-Kansas City 2021

ABSTRACT

Cerebral spinal fluid (CSF) is driven throughout the subarachnoid space (SAS) and serves a variety of crucial functions. The behavior of CSF within the optic nerve subarachnoid space (ONSAS) has special interest because it is relatively unknown. Additionally, the effects of improper flow characteristics of CSF within the ONSAS could be a contributing factor to optical neuropathies such as glaucoma. Rendering a three-dimensional model of the optic nerve (ON) and associated SAS can help provide a better representation of the physical boundary conditions that influence CSF flow. Utilizing this model, computational fluid dynamics (CFD) of the CSF within the ONSAS can be conducted to provide a visualization of the CSF behavior. In addition, flow rate and velocity of the ONSAS CSF can be calculated. Determination of the healthy velocity and volumetric flow rate of CSF within the ONSAS could help doctors to estimate ICP without utilizing invasive procedures such as lumbar puncture. The understanding of this flow within the ONSAS could provide medical professionals with more information prior to proceeding with invasive procedures and diagnosis of optic neuropathies. As a result, this study aims to establish a procedure for simulating the CSF flow within the ONSAS and determination of CSF velocity and volumetric flow rate.

APPROVAL PAGE

The faculty listed below, appointed by the Dean of the School of Computing and Engineering, have examined a thesis titled “Optic Nerve Subarachnoid Space Cerebral Spinal Fluid Computational Fluid Dynamics" presented by Vincent Levi Ryan Kent, candidate for the Master of Science degree, and certify that in their opinion it is worthy of acceptance.

Supervisory Committee

Amirfarhang Mehdizadeh, Ph.D.
Department of Civil and Mechanical Engineering

Antonis Stylianou, Ph.D.
Department of Civil and Mechanical Engineering

Ceki Halmen, Ph.D.
Department of Civil and Mechanical Engineering

CONTENTS

TABLES

ILLUSTRATIONS

ACKNOWLEDGEMENTS

I would like to extend my gratitude to Dr. Mehdizadeh for entrusting me with this research and providing his guidance all along the way. Additionally, I would like to sincerely thank Rohit Saini for all of the direction and assistance he imparted.

CHAPTER 1: INTRODUCTION

Cerebral spinal fluid (CSF) is driven throughout the subarachnoid space (SAS) and serves a variety of crucial functions. The behavior of CSF within the optic nerve subarachnoid space (ONSAS) has special interest because it is relatively unknown. There is a lack of understanding of the ONSAS CSF volumetric flow rate and how the CSF returns from the ONSAS due to the dead end geometry of the ONSAS. Additionally, the effects of improper flow characteristics of CSF within the ONSAS could be a contributing factor to optical neuropathies such as glaucoma. A three-dimensional model of the optic nerve (ON) and associated SAS can provide a better representation of the physical boundary conditions that influence CSF flow. Computational fluid dynamics (CFD) of the CSF within the ONSAS can provide a visualization of the CSF behavior. Understanding the flow within the ONSAS could provide medical professionals with more information prior to proceeding with medication injection, invasive procedures, and diagnosis of optic neuropathies

CHAPTER 2: BACKGROUND

The ON; a part of the central nervous system, is a white matter tract surrounded by CSF (Killer, Jaggi, Flammer, Miller, & Huber, 2006) and comprised of fibers made up of retinal ganglion cells (RGC) axons (Ireland & Carter, 2021). The ONSAS encloses around the entire length of the ON (Killer, Jaggi, Flammer, Miller, & Huber, 2006; Ohno-Matsui, et al., 2011), from the cranial cavity to the posterior globe (Morgan, et al., 2016). Terminated at the back of the eye, the ONSAS stops at the scleral flange (Ohno-Matsui, et al., 2011) which is located on the exterior of the ocular globe and reinforces and forms the eyes geometry (Killer, et al., 2007). The sclera flange serves as a link between the sclera and the ON head lamina cribrosa (Vurgese, Panda-Jonas, & Jonas, 2012). The lamina cribrosa supports the RGC axons as they enter the eye by supplying nutrients and reinforcement (Korbecki, Zimny, Podgorski, Sasiadek, & Bladowska, 2019).

Figure 1: Optic Nerve Anatomical Diagram

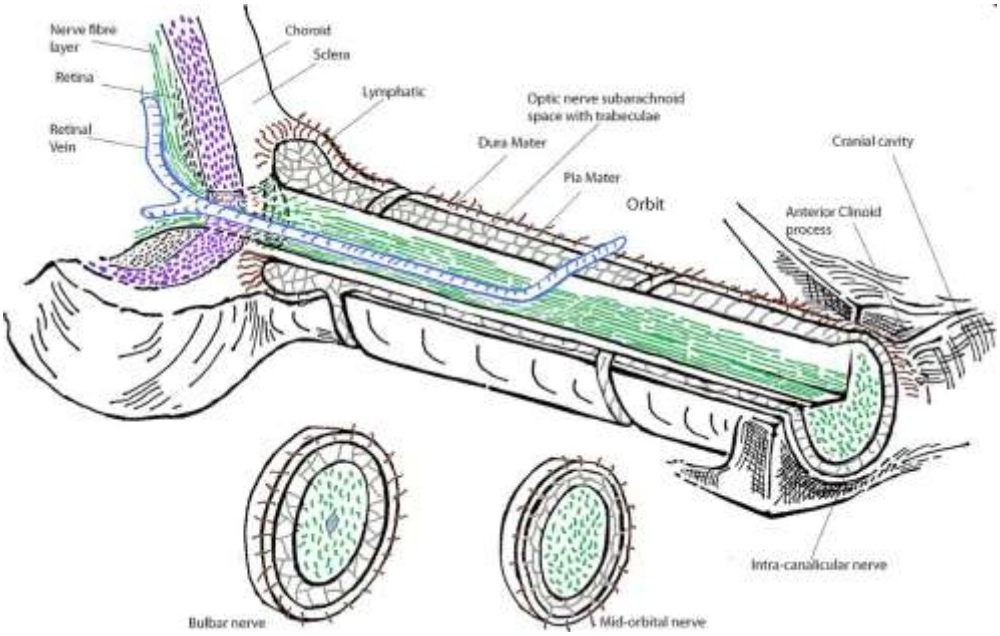

Note 1: Retrieved from *Cerebrospinal fluid pressure and the eye* (Morgan, et al., 2016)

The ON is enclosed by a meningeal casing known as the ON sheath and is comprised of the dura mater, arachnoid mater, and pia mater (Damor & Vatukiya, 2021). The dura mater is a layer of dense connective tissues (Shafique & Rayi, 2021) that encloses around a thin membrane. This membrane; arachnoid mater, separates the dura mater from the ONSAS and prevents CSF from passing into the dura mater (Shafique & Rayi, 2021). Adhering to the ON is a thin vascular layer called the pia mater (Shafique & Rayi, 2021) which is separated from the arachnoid mater by the SAS. The SAS is nonuniform in width along the length of the ON with the canalicular region of the ONSAS being the most slender (Killer, et al., 2007). Within the different regions of the ONSAS, an intricate system of tissue structures exist.

The ONSAS consists of a network of arachnoid trabeculae and septa in addition to CSF (Killer, Laeng, Flammer, & Groscurth, 2003). Arachnoid trabeculae are very thin reinforcement structures comprised of connective tissues (Shafique & Rayi, 2021). These arachnoid trabeculations within the ONSAS could serve as a resistor to CSF flow within the region if the network of these tissues is too dense (Liu & Michon, 1995; Morgan, et al., 2016). In addition to trabeculae, septa exists within the ONSAS. Septa are connective tissues (Bergen, 1982) that divide the ONSAS into sub compartments (Killer, Laeng, Flammer, & Groscurth, 2003). The ONSAS septa are thought to create an increased resistance to CSF flow (Morgan, et al., 2012). As the CSF flows through the ONSAS, it flows across the setae and trabeculae (Morgan, et al., 2016). This system of arachnoid trabeculae and septa are thought to heavily impact the CSF dynamics due to the bulbed dead end of the ONSAS (Killer, Laeng, Flammer, & Groscurth, 2003). Trabecula and

septa could allow CSF to flow into the ONSAS but act as a one-way flow valve that prevents reversed flow (Killer, Jaggi, Flammer, Miller, & Huber, 2006).

Figure 2: Schematic Representation of SAS Structure

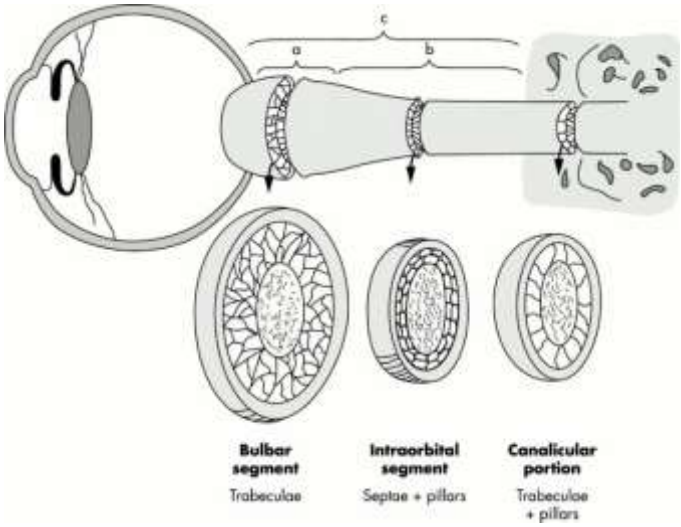

Note 2: Retrieved from *Architecture of arachnoid trabeculae, pillars, and septa in the subarachnoid space of the human optic nerve: anatomy and clinical considerations* (Killer, Laeng, Flammer, & Groscurth, 2003)

CSF is produced by the choroid plexus epithelium then travels to connecting compartments (Killer, Jaggi, Flammer, Miller, & Huber, 2006; Killer, 2013). After being produced, CSF proceeds to flow from the lateral ventricles to the third ventricle, then from the cerebral aqueduct to the fourth ventricle, and finally it reaches the brain SAS where it flows to the ONSAS (Killer, 2013). The CSF within the brain then connects with the ONSAS via the chiasmatic cistern (Li, et al., 2012) which resides within the SAS (Visual Loss: Disorders of the Chiasm, 2019). Once at the ONSAS, it is not fully understood how the CSF returns and is reabsorbed at the arachnoid villi since the CSF pressure gradient goes from the intracranial to the dead end ONSAS (Killer, Jaggi, Flammer, Miller, & Huber, 2006).

Figure 3: CSF Flow Path

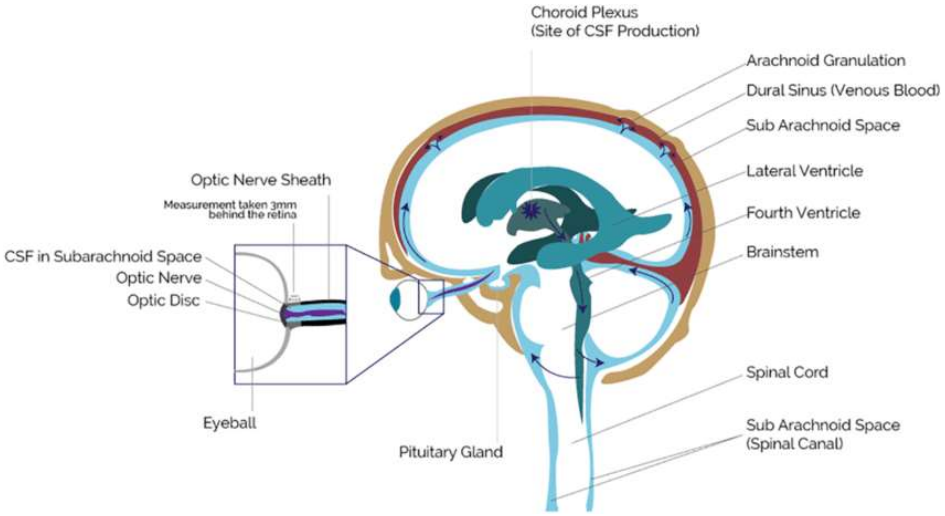

Note 3: Retrieved from *The role of optic nerve sheath diameter ultrasound in brain infection (Stead, et al., 2021)*

CSF is an ultrafiltrate of plasma (Telano & Baker, 2021) and assumed Newtonian fluid (Bloomfield, Johnston, & Bilston, 1998; Sharp, Carare, & Martin, 2019) that is thought to be homogenous in composition (Killer, et al., 2007; Killer, 2013). It has a dynamic viscosity of 1.1×10^-3 pascal-second and a density of 1.007×10^3 kilogram per cubic meter (Yatsushiro, Sunohara, Atsumi, Matsumae, & Kuroda, 2018). CSF contains proteins that are primarily (85%) derived from blood (Killer, Jaggi, Flammer, Miller, & Huber, 2006) and are thought to increase CSF viscosity when highly concentrated (Bloomfield, Johnston, & Bilston, 1998). CSF flow is thought to be continuous and equally distributed throughout the various CSF spaces (Killer, et al., 2007). After being produced in the choroid plexus (Morgan, et al., 2016) at a rate of 0.35 milliliters per minute (Wilson, 2016), CSF is driven through its circulatory path. Along this flow route, the CSF can be expressed as transient laminar flow (Sharp, Carare, & Martin, 2019). Throughout continuous circulation, between 400 and 600 ml of CSF is produced each day which enables 4 to 5 complete volumetric turnovers (Telano & Baker, 2021; Yatsushiro,

Sunohara, Atsumi, Matsumae, & Kuroda, 2018). The total volume of CSF within the various spaces of the cranial cavity is ~75 milliliters (Wilson, 2016).

The CSF flow propelling force is not entirely comprehended but is known to be influenced by multiple factors (Killer, et al., 2007). Of these factors, the CSF flow within the ONSAS surrounding the ON is dependent on the electrocardiogram (ECG) curve and respiratory rate (RR) interval (Boye, et al., 2018). The cardiac component of CSF flow is propelled by pulsations of arterial vessels (Yatsushiro, Sunohara, Atsumi, Matsumae, & Kuroda, 2018) which drives CSF backward during heart systole and forward during diastole (Korbecki, Zimny, Podgorski, Sasiadek, & Bladowska, 2019). The respiratory portion of CSF flow is driven by intrathoracic pressure change (Yatsushiro, Sunohara, Atsumi, Matsumae, & Kuroda, 2018). In addition to flow, CSF pressure within the ONSAS is effected by the cardiac and respiratory cycles (Morgan, et al., 2016). The ONSAS pressure and intracranial pressure (ICP) are thought to be homogeneous, with ICP translating to the ONSAS (Killer, Jaggi, Flammer, Miller, & Huber, 2006; Morgan, et al., 2012; Morgan, et al., 2016).

The normal range for intracranial pressure is between 5 and 15 mmHg (Morgan, et al., 2016; Nag, Swain, & Kant, 2019; Wilson, 2016). The ONSAS CSF pressure and ICP are equivalent when the ICP is above 0 mmHg (Morgan, et al., 2012). However, it has been shown in K9 experiments that ONSAS pressure has been found to be less than ICP (Hou, et al., 2016). Understanding that ICP is pulsatile (Morgan, et al., 2016; Nag, Swain, & Kant, 2019) and equal to ONSAS pressure (Killer, Jaggi, Flammer, Miller, & Huber, 2006; Morgan, et al., 2012; Morgan, et al., 2016), it is inferred that the pressure within the ONSAS is oscillatory. This would indicate that the ONSAS inlet has

alternating flow direction dependent on the ICP wave. The two primary components that drive fluctuating ICP is the respiratory and cardiac waves (Nag, Swain, & Kant, 2019). Additional factors thought to impact circulation of CSF throughout its path includes new CSF generation, body posture, brain piston action and vascular choroid plexus pulse pressure (Killer, et al., 2007).

ICP and CSF dynamics within the ONSAS are being investigated for their influence in optic neuropathy (Boye, et al., 2018) as it may be a result of lowered ICP (Hou, et al., 2016). Fluctuation in ICP correlates to the change in ONSAS width (Nag, Swain, & Kant, 2019) with the width increasing as the ONSAS CSF pressure does (Liu, et al., 2018). However, the reduction of the ONSAS width and impedance of CSF flow contribute to the compartmentation of the ON (Boye, et al., 2018). There is a low resistance relationship between the intracranial and ONSAS CSF (Morgan, et al., 2012). Additionally, a decrease of CSF flow within the ONSAS orbital section results in a subsequent decrease in CSF pressure (Boye, et al., 2018) and an irregular CSF flow rate could cause the buildup of harmful components and concentrated pathological proteins (Killer, Jaggi, Flammer, Miller, & Huber, 2006). Hindered CSF dynamics and decreased ICP may contribute to normal tension glaucoma (NTG) (Boye, et al., 2018). Patients with NTG have been shown to have reduced CSF flow along the ONSAS from the intracranial compartment (Morgan, et al., 2016).

Due to the limitations of current noninvasive medical procedures such as MRI, the velocity and volumetric flow rate of CSF within the ONSAS is not entirely known. Flow within other CSF compartments such as the cerebral aqueduct, have had more

CHAPTER 3: PROCEDURE

A magnetic resonance image (MRI) package was provided for the study by Dr. Peter Koulen from the University of Missouri-Kansas City Vision Research Center. Utilizing 2-Dimensional (2D) MRI images of the patients cranial space and a medical image processing software, the ONSAS CSF volume was extracted from each layer and rendered into an unrefined rough 3-Dimensional (3D) part. A computer aided design (CAD) software was used to inspect the volume and generate an average 2D ON and ONSAS profile. Using a computational fluid dynamic (CFD) software the CSF flow was simulated in the 2D ONSAS profile. Upon validation of the 2D model, the initial partially constructed 3D ONSAS was refined into a solid continuous volume using CAD software. After generating a complete model, simulation in CFD software was performed using the constructed 3D ONSAS. 2D and 3D simulation results were compared to establish consistency along with analyzing against researched experimental results.

CHAPTER 4: GEOMETRY RENDERING

An MRI was conducted and generated two-dimensional images of the cranial space in 1 mm increments for the three anatomical views: axial, sagittal, and coronal. The MRI package was uploaded to a medical image processing software; Slicer, and the ONSAS geometry was isolated from 17 consecutive image layers. Using the software, a level tracing effect was utilized to adjust color focus and intensity so the ONSAS could be isolated. The ONSAS of each layer and anatomical view (Figure *4*) was traced using a single pixel pen. Once the ONSAS geometry is traced for each layer, an unrefined 3D volume (Figure *5*) was rendered.

Figure 4: Optic Nerve Axial View

Figure 5: ONSAS Rendered Volume from MRI

The model generated from the medical imaging processing software was exported as a stereolithography file into the 3D CAD software; Solidworks. The imported ONSAS geometry was partitioned into 17 segments using planes. For each segment, the exterior (Figure 6) and interior edges (Figure 7) were traced using a spline generator until fully connected and enclosed 2D sketches were mapped on the outer surface boundary.

Figure 6: ONSAS Outer Diameter Profile

Figure 7: ONSAS In Diameter Profile

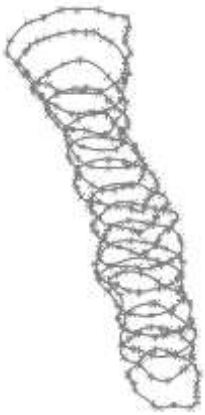

Once all sections were delineated, a design feature in the CAD program was used to generate a profile between each outside optic nerve sheath diameter (ONSD) surface sketch. Each surface sketch was selected and assigned a connector to control the interpolation between surface sketches. The connectors were adjusted into a linear sequence along the length of the imported part. Aligning connectors along the part profile generates a uniform surface profile when interpolating. Once interpolated, the part was cut away from the existing volume resulting in a solid body (Figure 8) representing the ONSAS and ON space.

Figure 8: Section View Of SAS & ON Cavity

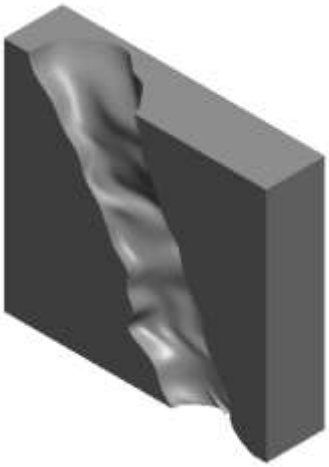

To isolate the ONSAS from the ON, the interior boundary lines for each segment was mapped utilizing the same method as described before. The CAD program was utilized to interpolate between the sketches to render a 3D profile, representative of the ON as shown in Figure 6. Therefore, the ON profile was lofted into the cavity shown in Figure 8. The resulting part conveys the cut away ONSAS volume (Figure 10).

Figure 9: 3D Optic Nerve

Figure 10: Section View Of ONSAS

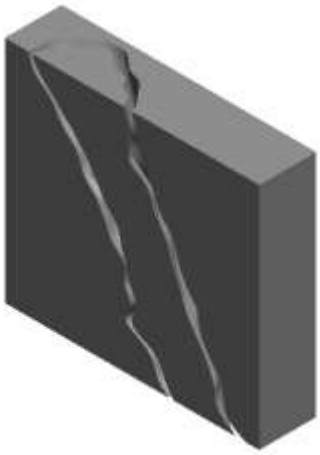

CHAPTER 5: 2D MODEL

The ONSAS geometry was segmented by planes into one millimeter increments. Partition cross sections were divided into four parts with the origin point being the center of the ON. For each partition, the radius of the ON and diameter of the ONSAS was measured for all four of the cross section divisions. These measurements were averaged to generate a mean ON diameter and ONSAS width for each partition. From these values, a 2D axisymmetric representation of the average ONSAS profile was developed.

Table 1: Average ONSAS & ON Profile

Distance From Eye Posterior (mm)	**ONSAS Average Width (mm)**	**ON Average Diameter (mm)**
17	0.447	3.75
16	0.569	3.53
15	0.597	3.61
14	0.473	3.87
13	0.375	3.96
12	0.542	3.93
11	0.439	3.92
10	0.449	3.92
9	0.528	3.84
8	0.605	3.55
7	0.486	3.94
6	0.536	3.58
5	0.525	3.41
4	0.502	3.96
3	0.392	4.48
2	0.554	5.41
1	0.524	5.90

From the average ON and ONSAS profile displayed in Table 1, it can be observed that as the ON diameter increases as it approaches the posterior of the eye. This larger portion of the ON is known as the bulbar region which is standardly larger in diameter than the rest of the ON. The average diameter of the modeled portion of the ON was determined to be 4.03±0.66 mm while the average ONSD was 5.04±0.74 mm. The

average width of the ONSAS is equivalent to half of the difference between the ON diameter and the ONSD. The average ONSAS width was determined to be 0.50±0.07 mm and the total length of the ON portion modelled is 17 mm.

Figure 11: ON & ONSAS Profile

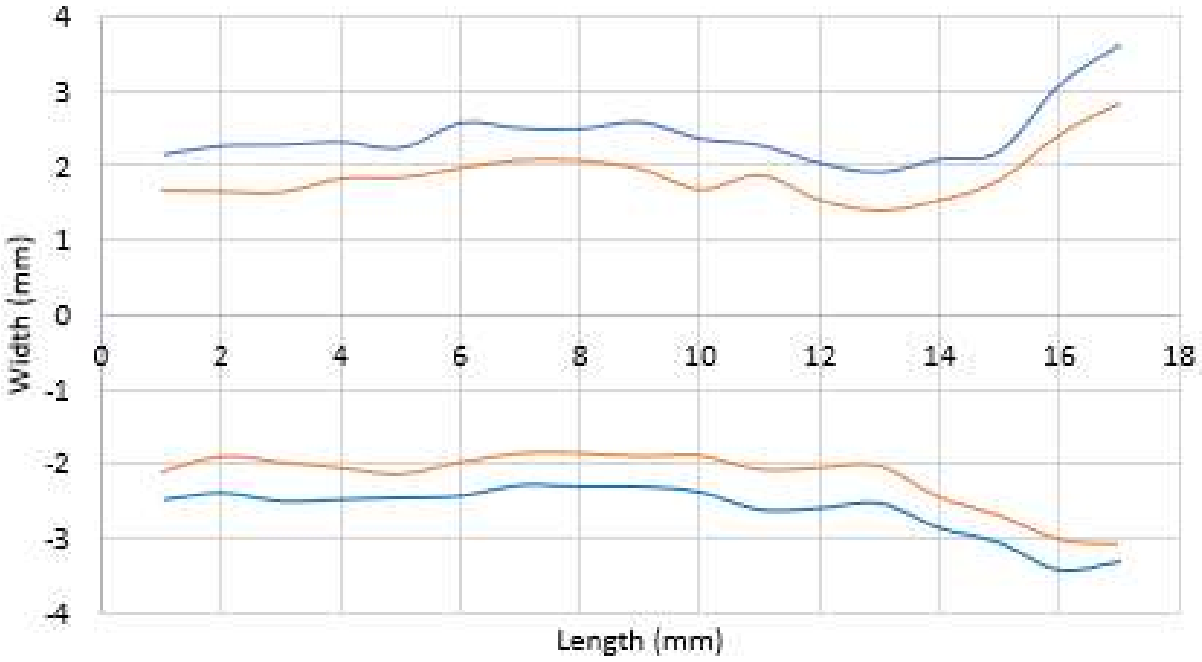

The average cross sectional area of the ONSAS was determined by modeling the system as a pipe and solving for the annulus area. The average cross section area of the ONSAS was calculated to be 0.05 cm^2.

$$A_{ONSAS} = \pi \cdot [\,(ONSD_{avg})^2 - (OND_{avg})^2]$$

To determine the viscous model, the Reynolds number is required to understand the flow regime. The Reynolds number was calculated by isolating the longitudinal cross section of the ONSAS and modelling it as a pipe. The average ONSAS width was used as the diameter of the pipe and the velocity was assumed to be equivalent to the experimental volumetric flow rate divided by double the ONSAS cross sectional area. This represents the velocity of both tracts of the ONSAS, for the left and right eye. The expected velocity

is near the CSF velocity range within the aqueduct. The average velocity of CSF within the aqueduct has been determined by experimental methods to be 2.42 cm/s (Ahmad, Salama, & Al-Haggar, 2021). The density and dynamic viscosity of CSF is determined to be 1007 kg/m^3 and 0.0011 kg/(m·s) respectively (Yatsushiro, Sunohara, Atsumi, Matsumae, & Kuroda, 2018). The average width of the ONSAS and subsequently the diameter used in calculating Reynolds number, was determined to be 0.5mm.

$$Re = \frac{\rho V D}{\mu} = \frac{\left(1007 \frac{kg}{m^3}\right)\left(0.0242 \frac{m}{s}\right)(0.0005m)}{(0.0011 \frac{kg}{m \cdot s})} = 11.14$$

Reynolds number was estimated to be 11.14 using the flow through a pipe assumption, which is less than 2300 and is considered as a laminar flow regime.

To generate a baseline understanding of the flow behavior within the ONSAS, the 2D profile was sketched in the CFD design software; Ansys Design Modeler. The sketch was conducted on the XY plane and the x-axis was utilized as the centerline of the ON so that the sketch would be axisymmetric. Once the sketch was enclosed and fully defined, the area between the enclosed edges of the sketch was designated as a surface body. The surface body geometry was then used to define and create the part. This surface body part is representative of the ONSAS and subsequently, the CSF flow region. To properly set the boundary conditions later in simulation setup, a named selection was utilized to define the starting edge of the 2D sketch as the inlet. A named selection was additionally used to define all remaining sketch edges as walls.

After initial setup, the profile was processed through a CFD meshing software; Ansys Mesher. Since the average thickness of the ONSAS was determined to be 0.5 mm, a sizing function was utilized to set element size to 0.01 mm. Setting this sizing results in

50 stacked quadrilateral elements within the average diameter of the ONSAS. Face meshing was then conducted to set the mesh method to quadrilaterals. Grid independence was determined by increasing the mesh size until the change in calculated velocity and pressure between mesh sizes was numerically zero. The total resulting elements within the profile was 21,508 and the total nodes within the meshed profile was 22,383.

Figure 12: 2D ONSAS Mesh

After the surface body was meshed, a CFD setup software; Ansys Fluent, was utilized to set boundary conditions and initialize simulation parameters. Initialization of the simulation required defining the inlet flow expression. Provided ONSAS pressure mirrors ICP, a pressure equation had to be developed to simulate the ICP waveform. The two primary components that drive fluctuating ICP is the respiratory and vascular pulse. The average adult RR is 14 breaths per minute while the average healthy adult heart rate (HR) is 80 beats per minute (Vital Signs (Body Temperature, Pulse Rate, Respiration Rate, Blood Pressure), 2021). The range of the respiratory and cardiac waves are 2-10 mmHg and 1-4 mmHg respectively with an average ICP range between 5 and 15 mmHg (Nag, Swain, & Kant, 2019). The respiratory pulse has the larger amplitude while the vascular pulse has the greater frequency.

$$ICP = A_{RR} \cdot \sin\left(\frac{RR}{60} \cdot 2\pi t - \frac{\pi}{2}\right) - A_{HR} \cdot \sin\left(\frac{HR}{60} \cdot 2\pi t + \frac{\pi}{2}\right) + A_{RR} + A_{HR} + ICP_{min}$$

The combined RR and HR components of the ICP wave shall not fall below 5 mmHg or exceed 15 mmHg. As a result, the allowable difference between maximum and

minimum is 10 mmHg. To accommodate this constraint, the combined amplitudes of the RR and HG waves shall be less than or equivalent to half of 10mmHg. Additionally, the difference between the maximum and minimum RR shall be greater than or equal to 2 mmHg but less than or equal to 10 mmHg. The minimum and maximum difference of the HR shall be between 1 and 4 mmHg. Therefore the RR amplitude was set to 3.75 mmHg while the HR amplitude was set to 1.25 mmHg.

For the ICP to conform to the upper and lower bounds; 5 and 15 mmHg, the waveform required a vertical shift. The shift is equal to 10 mmHg which is equivalent to the summation of the RR amplitude, HR amplitude, and minimum ICP. A phase shift was completed for both the RR and HR components of the waveform so that it intersects the minimum ICP value at time equal to zero. The angle variable; time, for the RR and HR sine components were multiplied by a correction factor to adjust the period of the waveform. The period of the waveform is equivalent to the time of a single respiratory

Figure 13: Simulated ICP Waveform

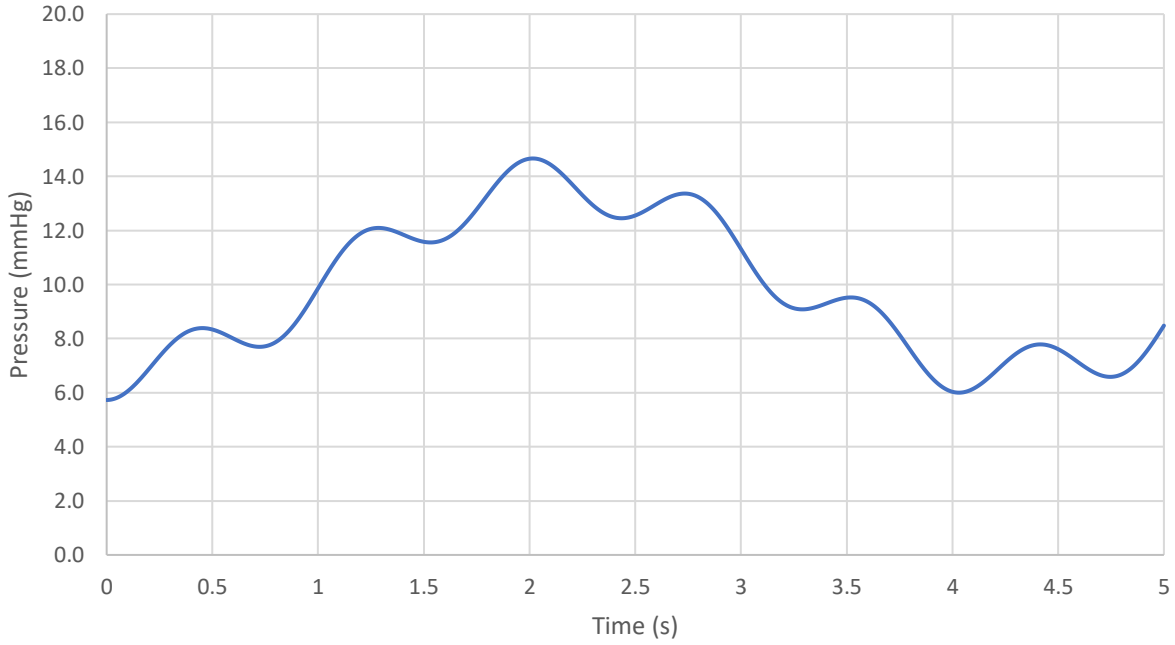

pulse. As a result, the waveform period is equivalent to a respiration rate of 14. Additionally, the frequency of the waveform was determined by multiplying the time variable for the RR and HR components by the respiratory pulse rate and vascular pulse rate respectively.

$$ICP = 3.75 \cdot \sin\left(\frac{14}{60} \cdot 2\pi t - \frac{\pi}{2}\right) - 1.25 \cdot \sin\left(\frac{80}{60} \cdot 2\pi t + \frac{\pi}{2}\right) + 10$$

The general setup of the simulations requires defining the solver type, velocity formulation, time state, space, and gravitational effect. Since the CSF flow is driven by ICP, the simulation was set to a pressure based solver type. The velocity formulation was set to absolute rather than relative due to the non-rotational flow of the domain. The time is specified as transient given the inlet condition is contingent upon the derived equation for ICP which is time dependent. The space is defined as planar since the imported part is a 2D surface body. The gravitational effects is neglected since the driving component of flow is fluctuation in ICP which already takes into consideration gravitational effects.

The simulation setup requires a model determination to utilize. Therefore, a viscous model is established as laminar due to the calculated Reynolds number. Once the model type is determined, the CSF material type must be setup as a new fluid type defined by density and viscosity. Upon defining the CSF, the cell zone fluid conditions assigned the surface body zone as CSF. The CSF has to have clearly defined parameters so the boundary conditions had to be designated for the inlet, internal, and wall.

The inlet and walls were defined by momentum conditions since the primary results being investigated is pressure, velocity, and volumetric flow rate. A gauge total pressure expression equivalent to the derived ICP waveform (Figure 13), defined the inlet boundary condition. It is assumed that the walls of the ONSAS does not significantly

deform under normal ICP conditions so the walls were designated as stationary. Additionally, it is assumed that the arachnoid mater and pia mater are solid boundaries so the no slip shear condition was applied to the walls.

To monitor and validate the inlet pressure expression, a report definition was created to establish reportable area-weighted average static pressure. Reporting the pressure value required setting up a report file to acquire data from each time step of the simulation and print to the console. To view the collected data, a report plot had to be established. The real time report plot graphed the report file data for every time step. The graph displayed the flow time versus the weighted average of static pressure. After the simulation completed, the report plot was overlayed (Figure *14*) on the derived ICP graph to determine accuracy.

Figure 14: Simulation Inlet Pressure & ICP Waveform Superimposed

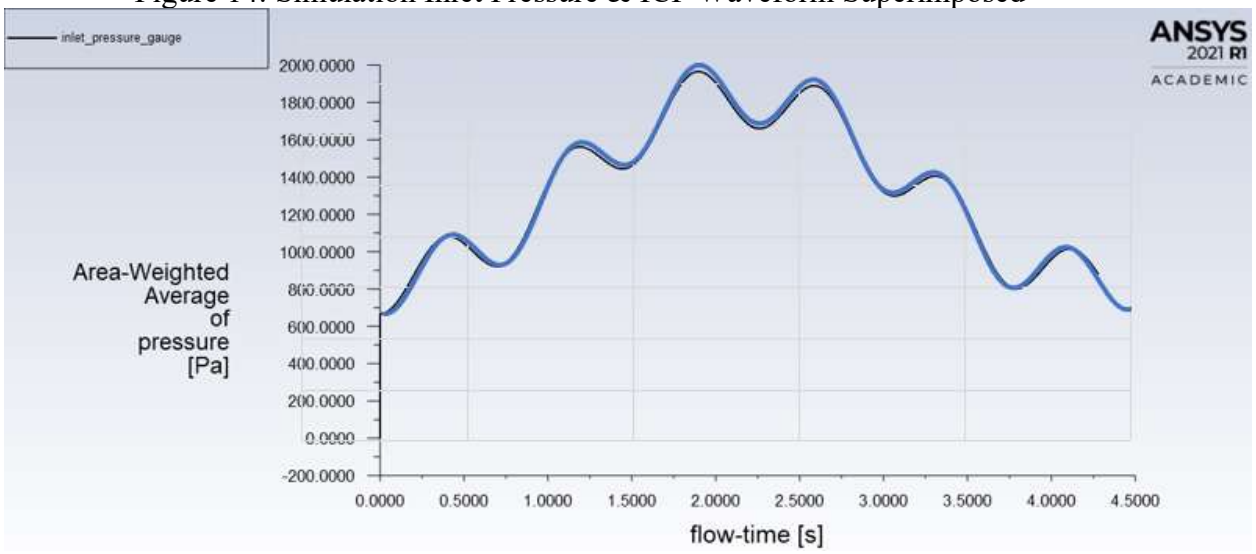

Before calculation activities could be conducted, the simulation had to be initialized. A standard initialization was selected and the solution was set to compute from the inlet. The initial inlet conditions had to be set prior to calculation. The ONSAS planar surface is located in the XY plane with the inlet being perpendicular to the x-axis.

Therefore the initial vertical velocity component is equivalent to zero. The software automatically calculated the inlet x-velocity to be 1.15 m/s based upon the geometry and inlet pressure expression. This is expected since the horizontal velocity is parallel to the x-axis and the inlet pressure expression is greater than zero.

Prior to initiating simulation, the time advancement and solution processing parameters were defined. The time advancement was defined as a user specified fixed type with 42,800 time steps of 0.1 ms size. Each time step had 20 maximum iterations with a single reporting and profile update interval. Solution processing data sampling for time statistics was turned on for a sampling interval of one. Upon setting these parameters, the solution was advanced to calculate.

CHAPTER 6: 3D MODEL

To simulate the CSF flow, the ONSAS had to be isolated using a CAD software; Solidworks. Utilizing the outside ONSAS diameter shown in Figures 4, a volume was rendered by interpolating between each profile sketch layer. The resulting part is representative of the ONSAS and ON as a solid body. The ONSAS inside diameter profile shown in Figure 5, was used to cut the ON volume from the ONSAS and ON solid body. This resulted in an isolated ONSAS volume with an unrefined dead end geometry. A constant size fillet was applied to the inner and outer edges of the ONSAS dead end geometry to generate a rounded termination of the ONSAS (Figure *15*). The filleted end more accurately represents the ONSAS geometry displayed on the MRI that the medical image processing software single pixel pen was unable to capture.

Figure 15: CFD Fluid Volume

The refined 3D model generated in the CAD software was imported as a parasolid into the CFD compatible CAD design software. Part volume was automatically assigned as the fluid body when imported into the software. The inlet and walls were assigned by named selections to define the geometric boundary conditions. The inlet was defined as the start of the cross section of the ONSAS and the ONSAS outer diameter was

designated as a wall. Upon completing initial model setup, the model was meshed inside of a CFD meshing software.

Figure 16: 3D ONSAS Mesh

Figure 17: 3D ONSAS Mesh Cross Section View

Meshing was performed on the part utilizing an automatic method of tetrahedron elements. Tetrahedron method was chosen due to the complex geometry of the part and its ability to refine mesh quality. Mesh sizing was performed to set a 0.255 mm element size which generated a fine mesh and element quantity that optimized computation time and accuracy. The total nodes and elements produced by this method was 18,850 and 80,536 respectively. After completing part meshing, the model was opened in a CFD setup software.

The general setup of the simulation required defining the solver type, velocity formulation, time state, and gravitational effect the same as the 2D simulation. Resembling the 2D simulation, the viscous model was set as laminar and the CSF was established as a new fluid type. The fluid space was defined as the 3D volume of the imported part. The cell zone fluid conditions assigned the part body zone as CSF. The CSF has to have clearly defined parameters so the boundary conditions had to be designated for the inlet, internal, and wall. These parameters were set by replicating the

2D simulation setup. Additionally, a report file and plot was established to graph the pressure at the inlet. After the simulation completed, the report plot was overlayed on the derived ICP graph to determine accuracy.

Before calculation activities could be conducted, the simulation had to be initialized. A standard initialization was selected and the solution was set to compute from the inlet. The initial inlet conditions had to be set prior to calculation. The ONSAS inlet surface is located in the XY plane with the inlet surface being perpendicular to the z-axis. Therefore the initial x-velocity and y-velocity components are equivalent to zero. The software automatically calculated the inlet z-velocity to be 1.15 m/s based upon the geometry and inlet pressure expression. This is expected since the z-velocity is parallel to the x-axis and the inlet pressure expression is greater than zero. Post initializing the simulation, the calculation parameters were replicated from the 2D simulation.

Figure 18: Inlet Z-Velocity Component

CHAPTER 6: RESULTS

The average velocity magnitude of the CSF flow within the 2D ONSAS is 26.90 μm/s. Compared to experimental values of CSF flow within compartments prior to the ONSAS, the velocity is multiple orders of magnitude less than expected. One explanation to this is that the dead end geometry paired with the pulsatile flow results in an averaged value of forward and backward flow. For flows with alternating direction, root mean squared error (RMSE) velocity will provide an average velocity regardless of flow direction. The simulation calculated RMSE velocity magnitude of the CSF is 0.556 cm/s and will be referred to as the average absolute velocity magnitude from here on. From experimental data, the CSF volumetric flow rate within a compartment prior to the ONSAS was determined to be between 2.98 and 9.42 ml/min (Ahmad, Salama, & Al-Haggar, 2021). Knowing the average absolute velocity magnitude and average cross sectional area of the ONSAS, the average volumetric flow rate could be calculated. The calculated average volumetric flow of the 2D profile was 1.97 ml/min.

Figure 19: 2D ONSAS Average Velocity Magnitude

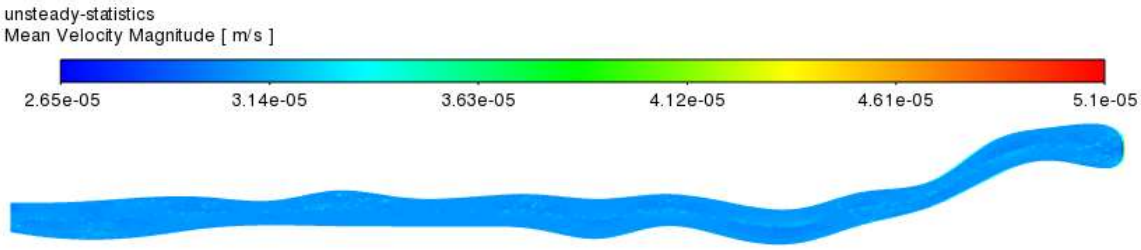

The average static pressure within the ONSAS is determined to be 1340.637 Pa (10.05 mmHg). The average pressure of the ICP waveform first period is 1337.046 Pa (10.03 mmHg). The CFD calculated average static pressure of the ONSAS is 2.69% higher than the average pressure of the inlet pressure expression. This difference in

pressure could be due to the change in width along the profile of the ONSAS. Additionally, the dead end geometry of the ONSAS prevents continuous flow of CSF which could increase the pressure within the surface body. If reversed flow through the inlet is not equivalent to forward flow, the amount of fluid increases within the ONSAS which increases pressure. Due to the stationary walls, the width of the ONSAS cannot increase. Therefore, the pressure inside of the ONSAS will increase when the inlet forward flow is greater than the inlet reverse flow.

Figure 20: 2D ONSAS Average Static Pressure

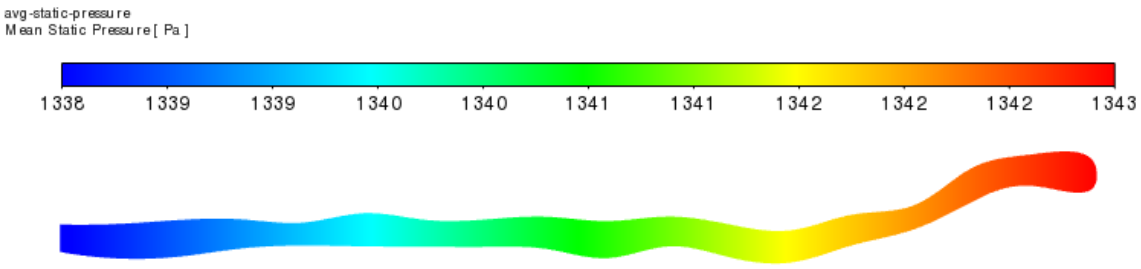

Simulation of the 3D model generated an average static pressure contour (Figure *21*) with strong correlation to the 2D simulation. Average static pressure of the 3D model over one period of the ICP waveform was calculated to be 1340.967 Pa (10.058 mmHg). This is a minuscule 0.02% difference compared to the 2D average static pressure. Both models have an average static pressure that falls within the expected average ICP range. Validation of the average static pressure incorporated verification of the inlet pressure expression. To verify the inlet pressure with respect to time, the ICP waveform was superimposed onto the gauge pressure expression report plot. The resulting graph was identical to the 2D superimposed pressure plot (Figure *14*).

Figure 21: 3D ONSAS Static Pressure Contour

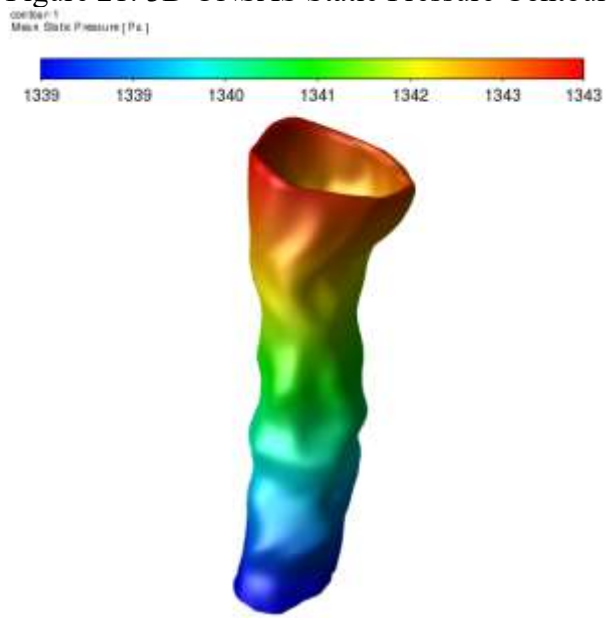

Average velocity within the fluid volume was determined to be a minimal 85.97 μm/s. This velocity is an average over a single period of the ICP waveform. Over this sole period, flow within the ONSAS space fluctuates between forward and reverse. The averaging of forward and reverse flow results in a mean velocity close to naught. The non-directional dependent average absolute velocity magnitude was calculated to be 0.652 cm/s. This indicates that CSF flows forward at an average of 0.652 cm/s and then backward at the same rate. This velocity is 17.2% higher than the 2D simulation determined RSME velocity. One possible explanation for this is the non-uniform geometry of the 3D model and the increase in number of thin ONSAS locations. To maintain the same volumetric flow rate through these reduced width areas, velocity must increase. To calculate the volumetric flow rate, the average ONSAS cross sectional area was multiplied by RSME velocity. The average ONSAS cross sectional area is 0.05 cm^2 and the RSME velocity is 0.652 cm/s so the resulting volumetric flow rate is determined to be 1.97 ml/min.

Figure 22: 3D ONSAS Velocity Contour Section View

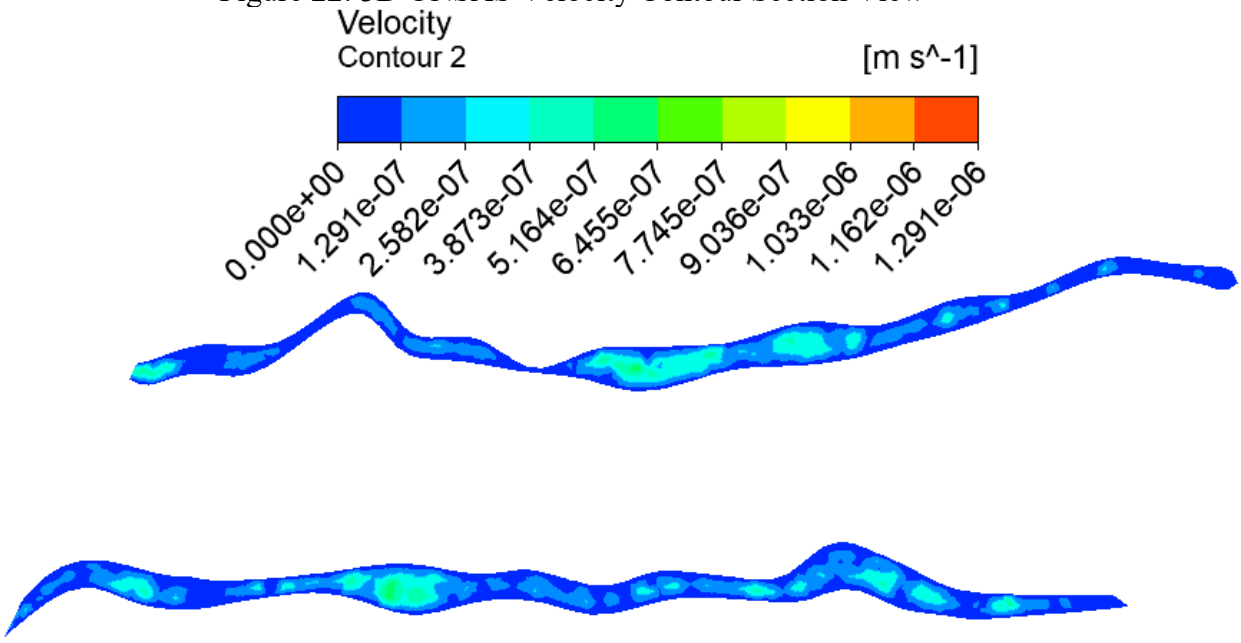

CHAPTER 7: CONCLUSIONS

From the simulated CSF flow within the 3D ONSAS, it can be interpreted from the velocity contour (Figure *22*) that the CSF does not have a clear flow turnaround. The CSF is consistently propelled forward and backward along the ONSAS causing pockets of mixing to develop in the sections with greater width. Upon entering the ONSAS, a CSF particle will continue to flow back and forth until it eventually gets absorbed by the lymphatics or revered back into the SAS prior to the ONSAS. This system resembles the way in which waves push water towards the beach but yet many of those water particles make it near the beach but end up being pulled back out to the ocean.

The frequency of the RR and HR impact the flow of the CSF within the ONSAS. Increases in RR and HR, such as conducting physically exerting activities, could increase the turnover rate of CSF within the SAS. Stagnant CSF particles could become removed from their compartment and propelled back into the circulatory path. Given the pulsatile flow of CSF and the dead end geometry of the ONSAS, segregation of the ONSAS due to thick or damaged arachnoid trabeculae and septa could isolate the CSF creating a buildup of proteins and toxins. An increase in concentration of these components could alter the fluid properties of the CSF within these isolated sections. Maintaining a healthy flow through the ONSAS compartment is critical to avoid buildup of harmful components. Therefore, volumetric flow rate of CSF plays a key role in maintaining the turnover of CSF within the ONSAS.

The average area of the cerebral aqueduct is 0.04 cm2 with an average CSF average absolute velocity magnitude between 1.99 and 2.86 cm/s (Ahmad, Salama, & Al-Haggar, 2021). Average ONSAS CSF absolute velocity magnitude obtained from the 2D

and 3D simulations were 0.56 and 0.65 cm/s respectively. The 3D simulated velocity is 67% lower than the minimum bound of the velocity retrieved from Ahmad et al. An explanation for the lower velocity comes from the understanding that the aqueduct does not have a dead end geometry such as the ONSAS. This geometry is hindering to the development of the velocity profile along the ONSAS which reduces the maximum velocity achieved.

The CSF flows through the aqueduct and succeeding compartments before reaching the optic chiasm and splitting into separate ONSASs for the oculus sinister and oculus dexter. Therefore the velocity of the CSF will vary from the aqueduct velocity but the total volumetric flow rate of the left and right ON ONSAS should be relatively similar to the flow rate within the aqueduct. Though the CSF velocity of the aqueduct and ONSAS are not thought to be equivalent, the comparison provides an extent of reliability for the simulated results.

The volumetric flow through a 0.04 +/- 0.015 cm2 CSF aqueduct is between 2.98 and 9.42 ml/min with an average of 5.81 ml/min (Ahmad, Salama, & Al-Haggar, 2021). The average cross sectional area of the ONSAS was 0.05 cm2 which is within the standard deviation of the aqueduct area calculated by Ahmad et al. Provided the CSF flows from the aqueduct and fourth ventricle into the SAS, the ONSAS should be less than half the expected volumetric flow rate since the SAS splits into two separate ONSAS tracts with equivalent cross sectional areas to the aqueduct.

Assuming that each ONSAS has the same cross section area and angle of connection to the junction, halving the aqueduct volumetric flow rate will provide the anticipated upper limit for volumetric flow rate of a single ONSAS. Assuming that fluid

is lost along the SAS route to absorption, compartments, and cavities, the anticipated volumetric flow rate of a single ONSAS is less than 2.91 ml/min. Therefore, the expected volumetric flow rate of a single ONSAS lies between 1.49 and 2.91 ml/min while the calculated flow rate of the 3D model was 1.97 ml/min. This flow rate is less than the average 2.91 ml/min but greater than the 1.49 ml/min lower bound. The 2D simulation produced a volumetric flow rate of 1.68 ml/min which also falls below the average but surpasses the lower threshold. Utilizing the method outlined in this paper, the volumetric flow rate of the ONSAS is determined to be 1.97 ml/min.

Table 2: Pressure, Velocity & Flow Rate Values

	2D Simulation	3D Simulation	Available Literature Data
Mean Static Pressure [mmHg]	10.05	10.06	5 - 15
Average Absolute Velocity Magnitude [cm/s]	0.56	0.65	1.99 – 2.86
Volumetric Flow Rate [ml/min]	1.68	1.97	1.49 – 4.71

Determining the average absolute velocity magnitude and ONSAS cross sectional area can provide doctors with an insight into the expected values for healthy patients. Continued development of invasive procedures such as velocity encoded phase contrast imaging can be paired with MRI utilization to calculate the ONSAS average area. Utilizing the results the CSF volumetric flow rate range of patients can be determined. This study determined the ONSAS RSME velocity and volumetric flow rate of a patient with healthy ICP. Using the existing non-invasive methods for determining velocity of CSF and area of ONSAS, the calculated volumetric flow rate can be used to compare against the simulation values of this study. Comparison of volumetric flow rates can

provide doctors with an invasive method of determining ICP without utilizing invasive methods such as lumbar puncture.

CHAPTER 8: FUTURE WORK

If the method employed in this paper was replicated for a control group of healthy individuals, an average volumetric flow rate could be calculated for the ONSAS. This additional study would have an ECG conducted for each patient along with an ICP measurement. From these values, an individual ICP waveform would be generated for each patient to match their ICP, HR, and RR. The resulting volumetric flow rate would be calculated and associated with their ICP, ONSAS width, HR and RR.

APPENDIX

Figure 23: MRI Axial View

Figure 24: MRI Coronal View

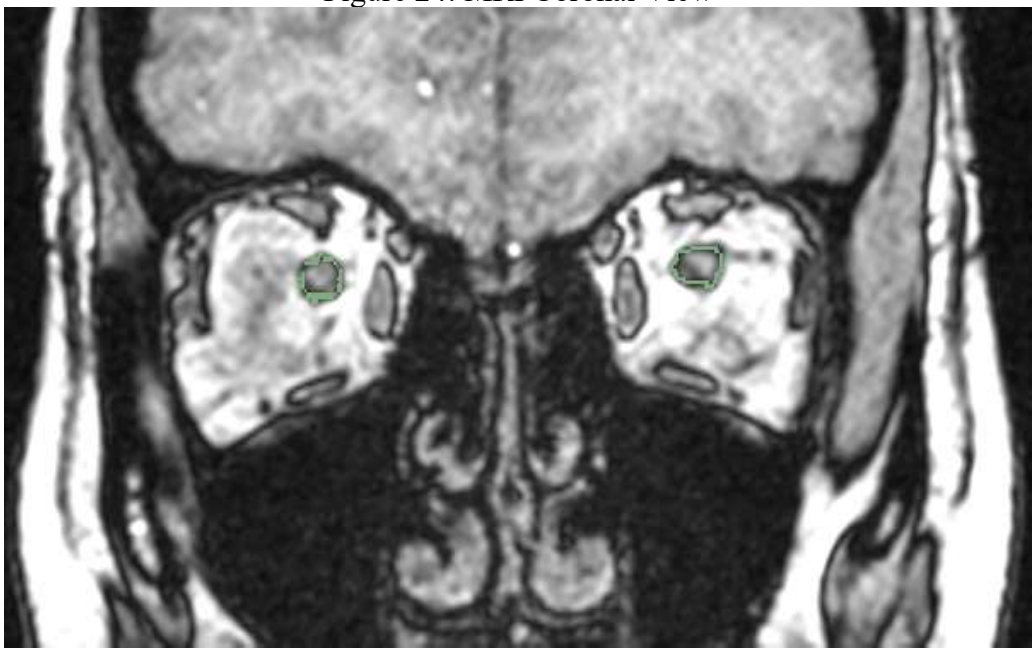

Figure 25: MRI Sagittal View

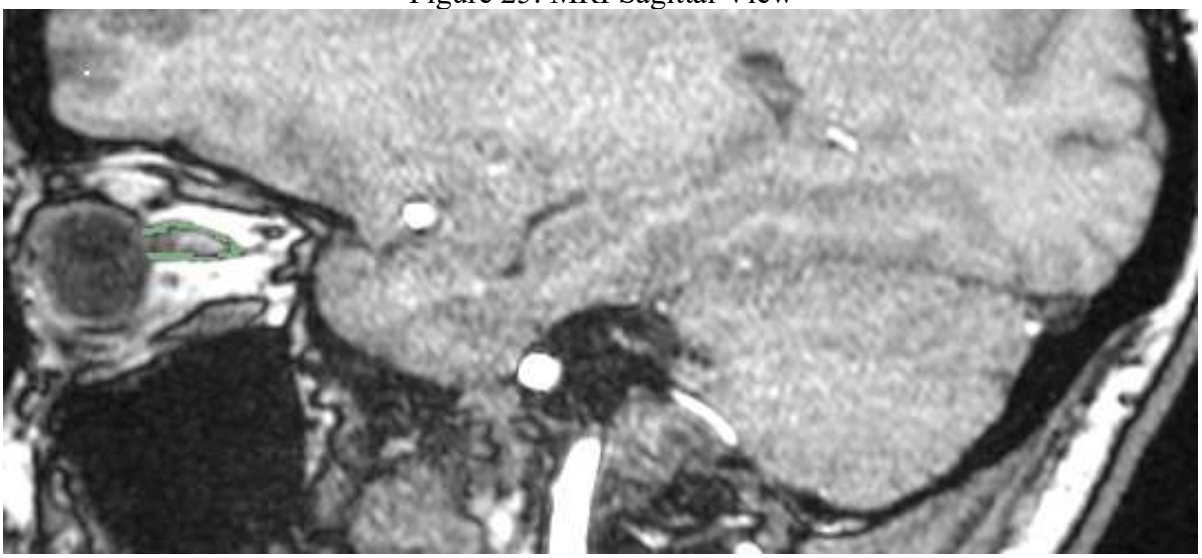

Figure 26: Dimensioning of 2D ONSAS

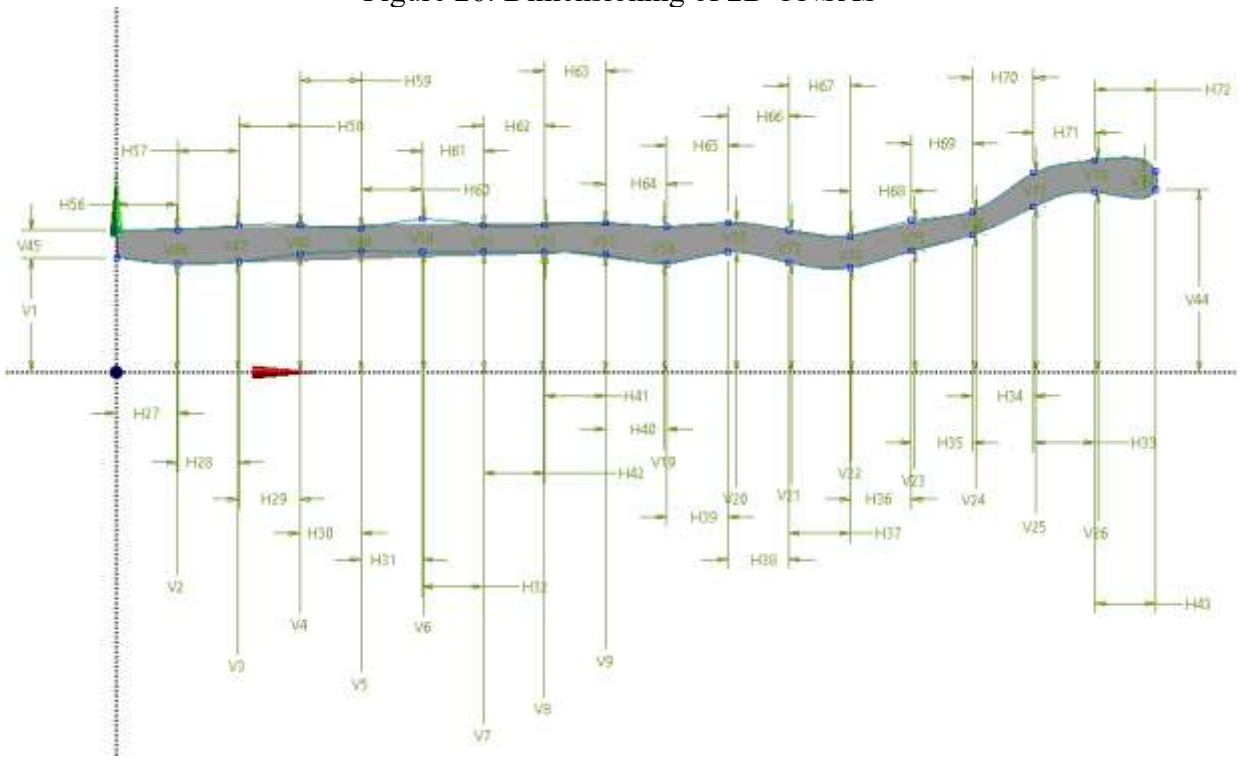

Figure 27: 3D Simulation Residuals

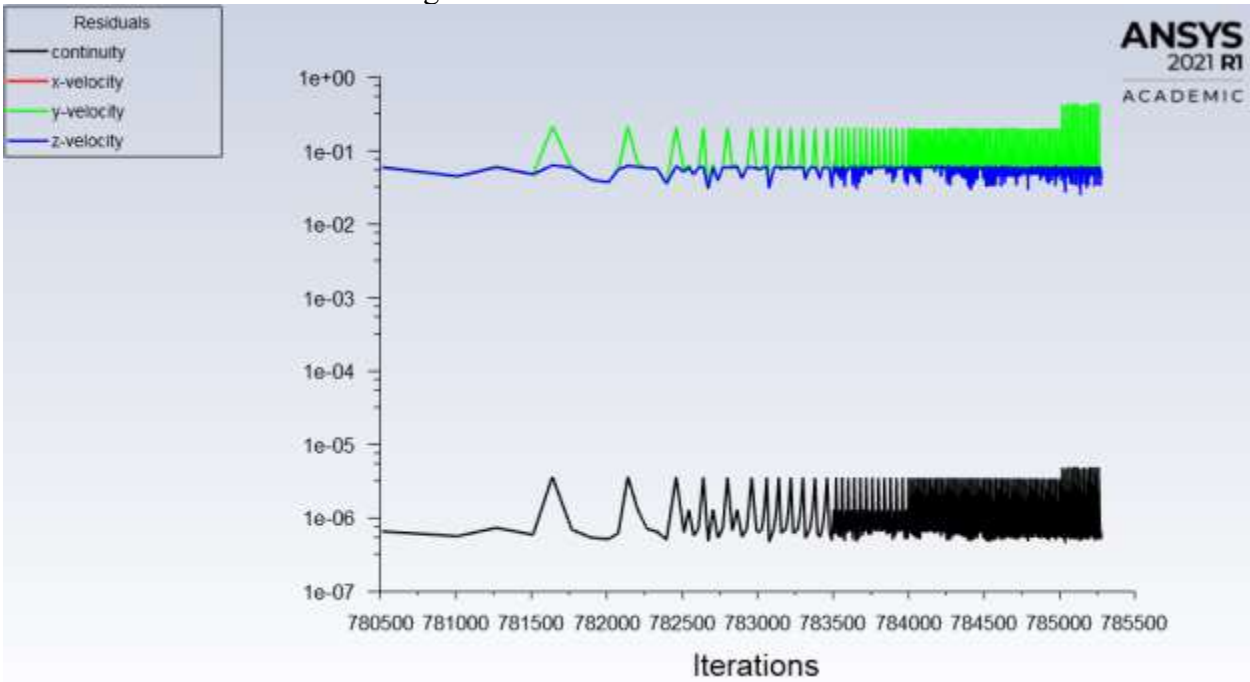

Figure 28: Viscous Model Setup

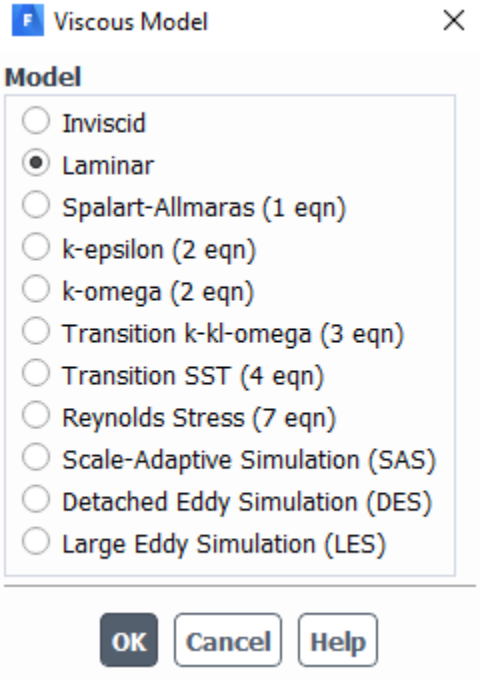

Figure 29: General Simulation Setup

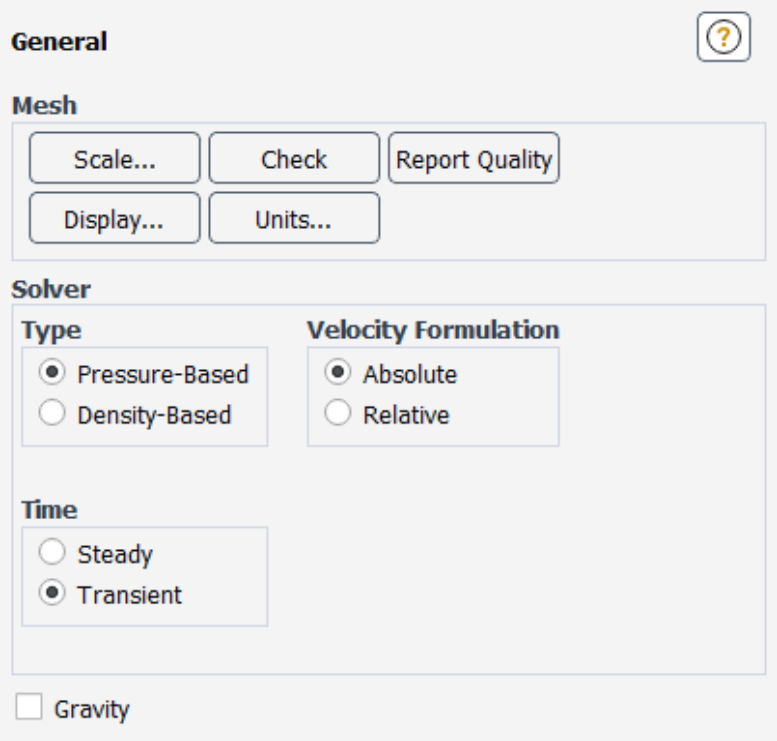

Figure 30: Material Type Setup

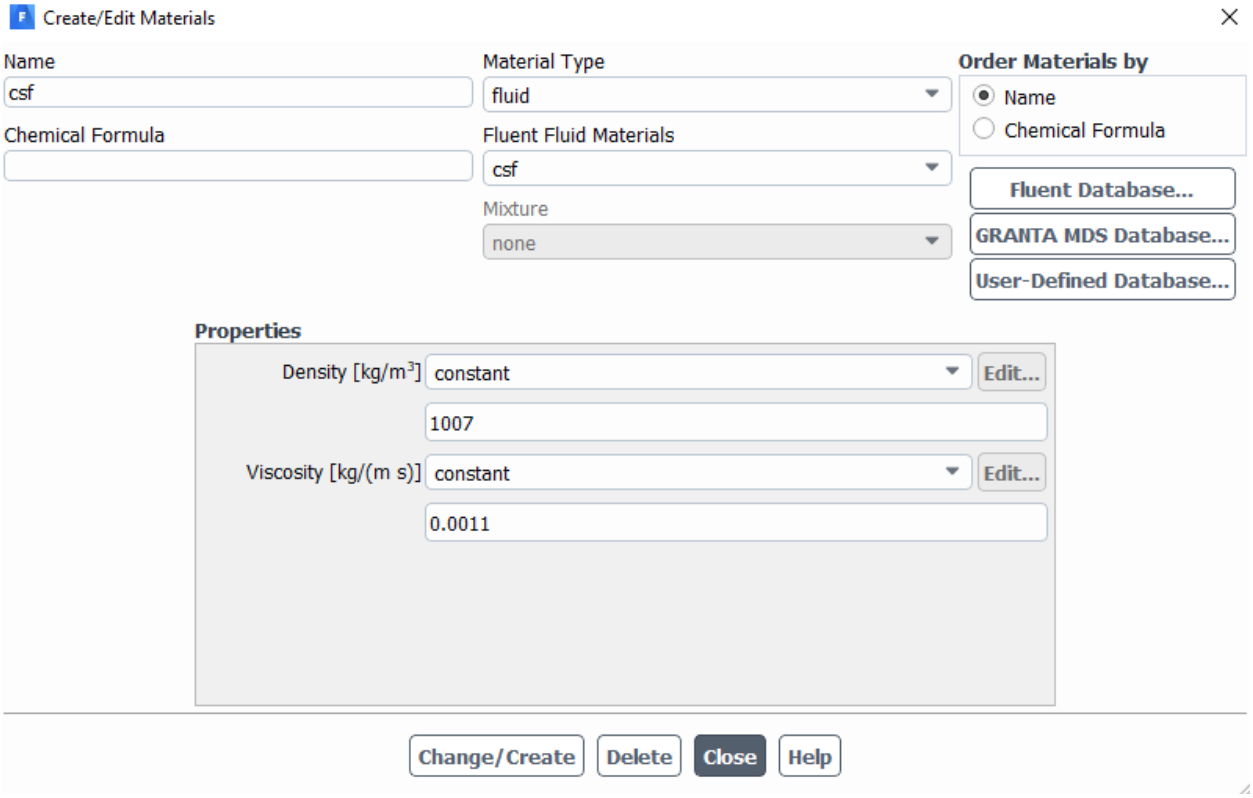

Figure 31: Inlet Condition Setup

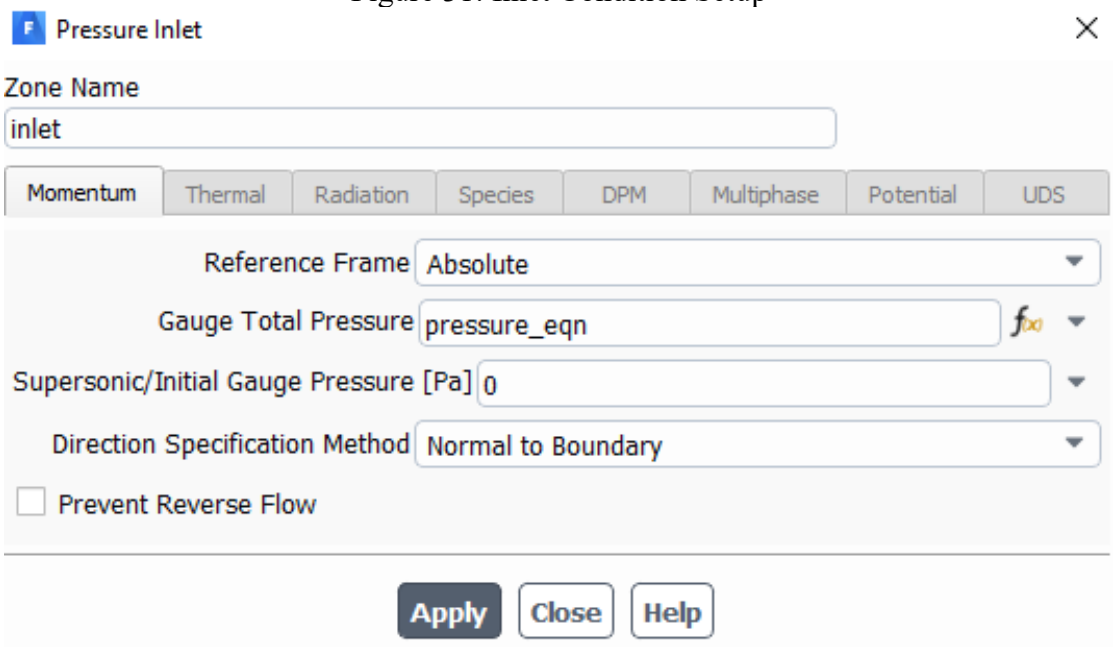

Figure 32: Wall Condition Setup

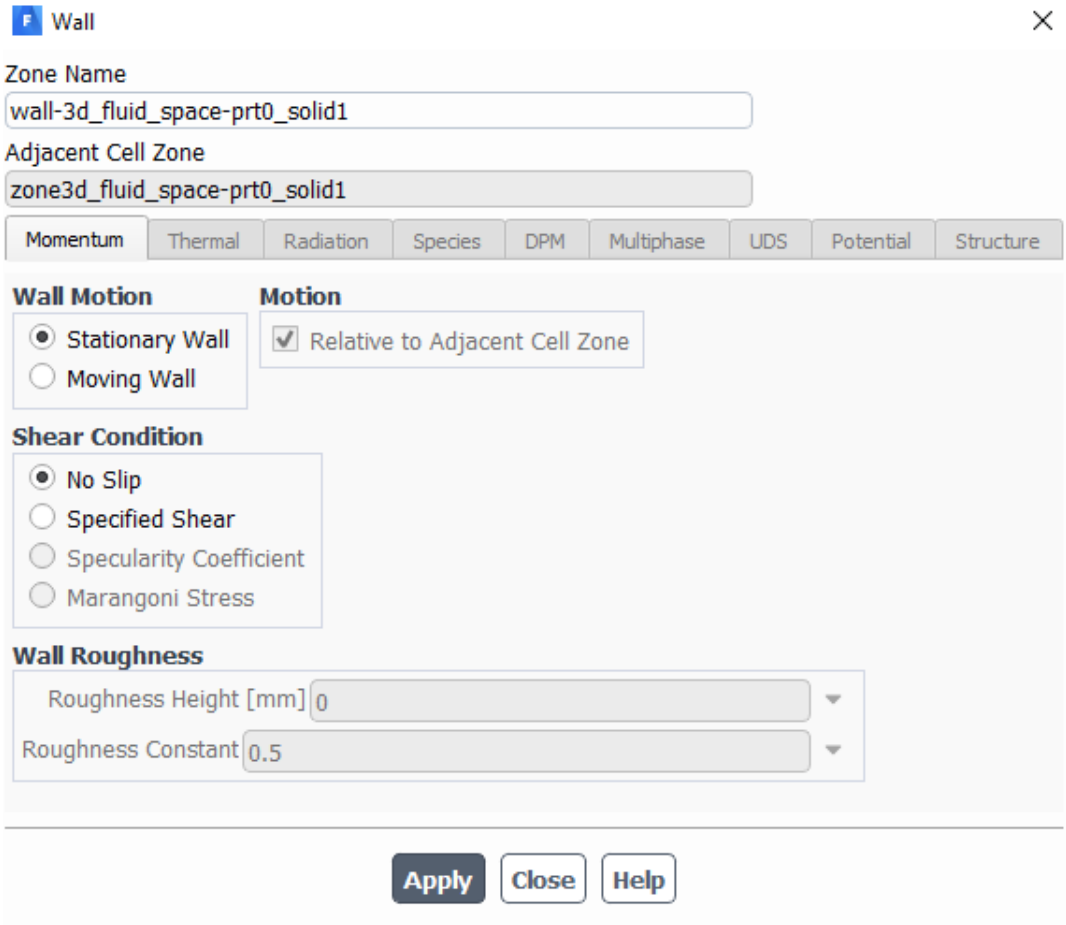

Figure 33: Named Expression Setup

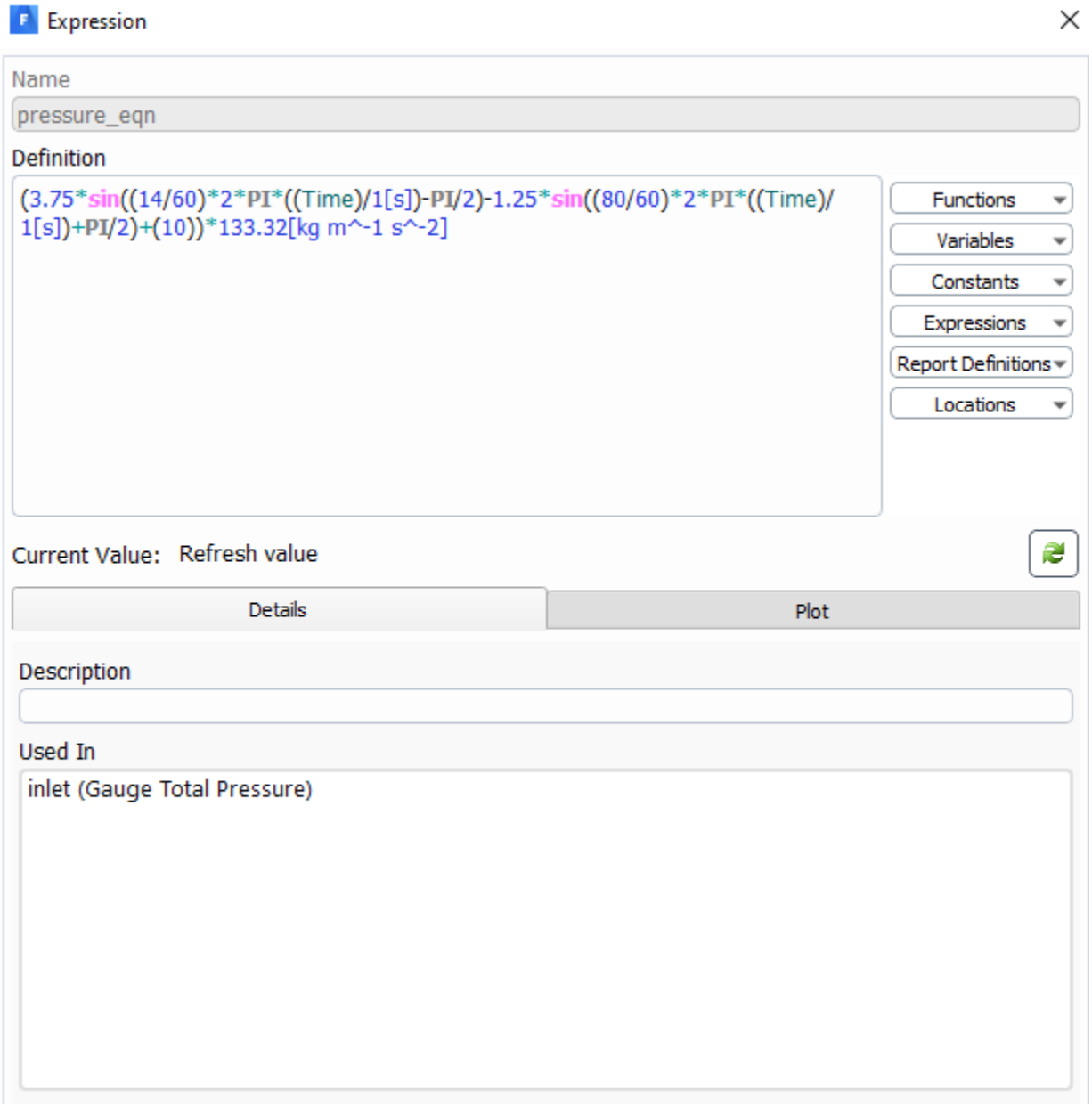

Figure 34: Surface Report Definition Setup

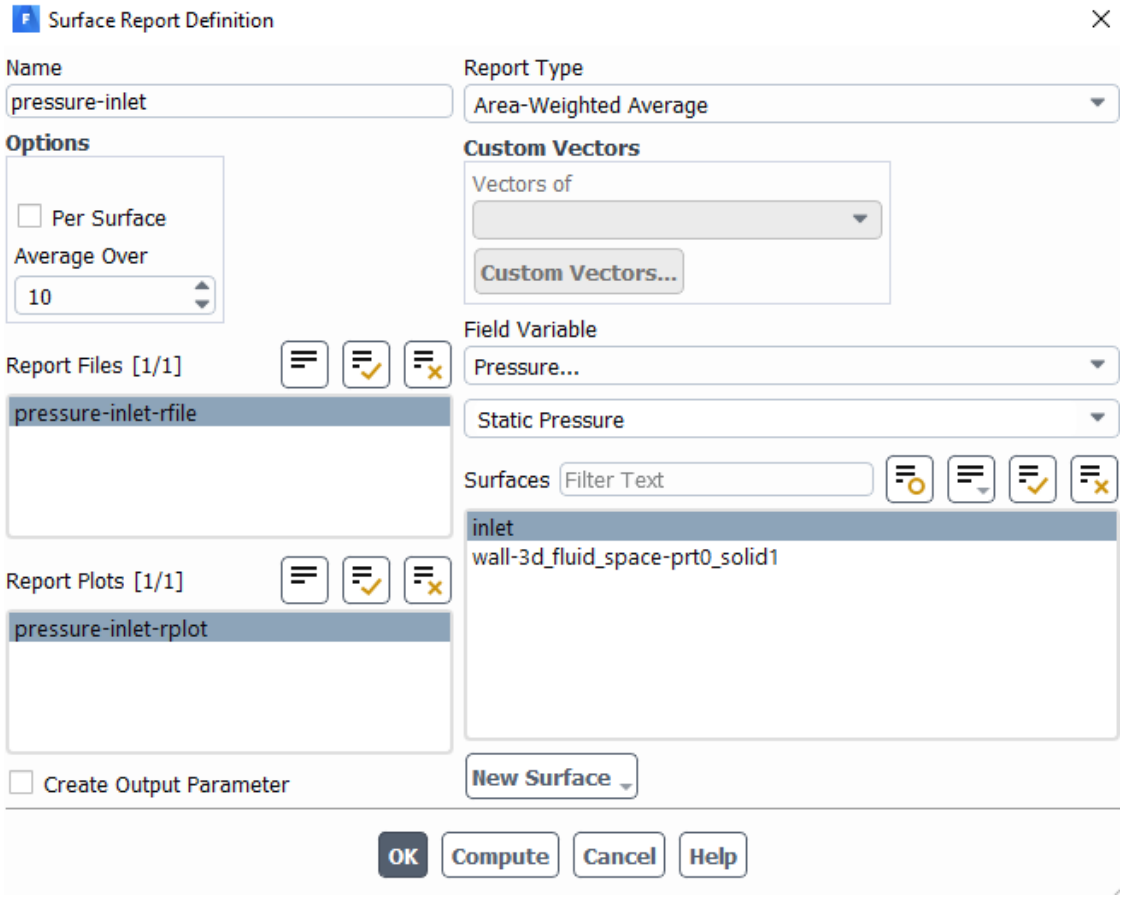

Figure 35: Report File Setup

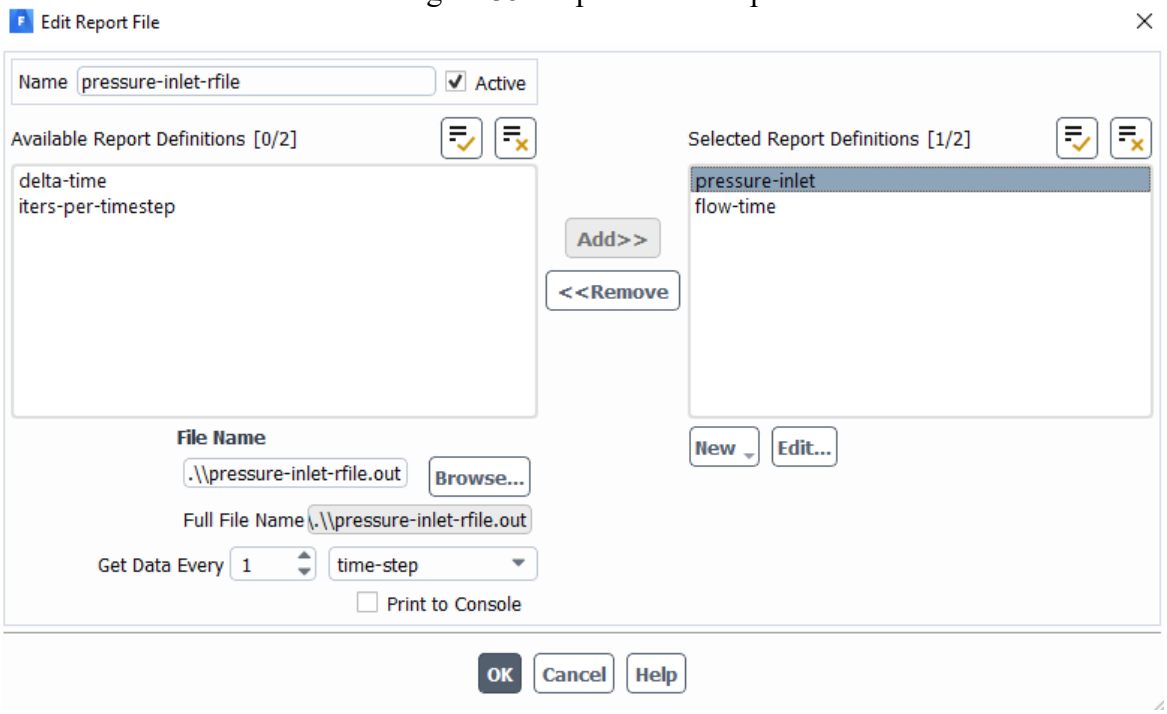

Figure 36: Report Plot Setup

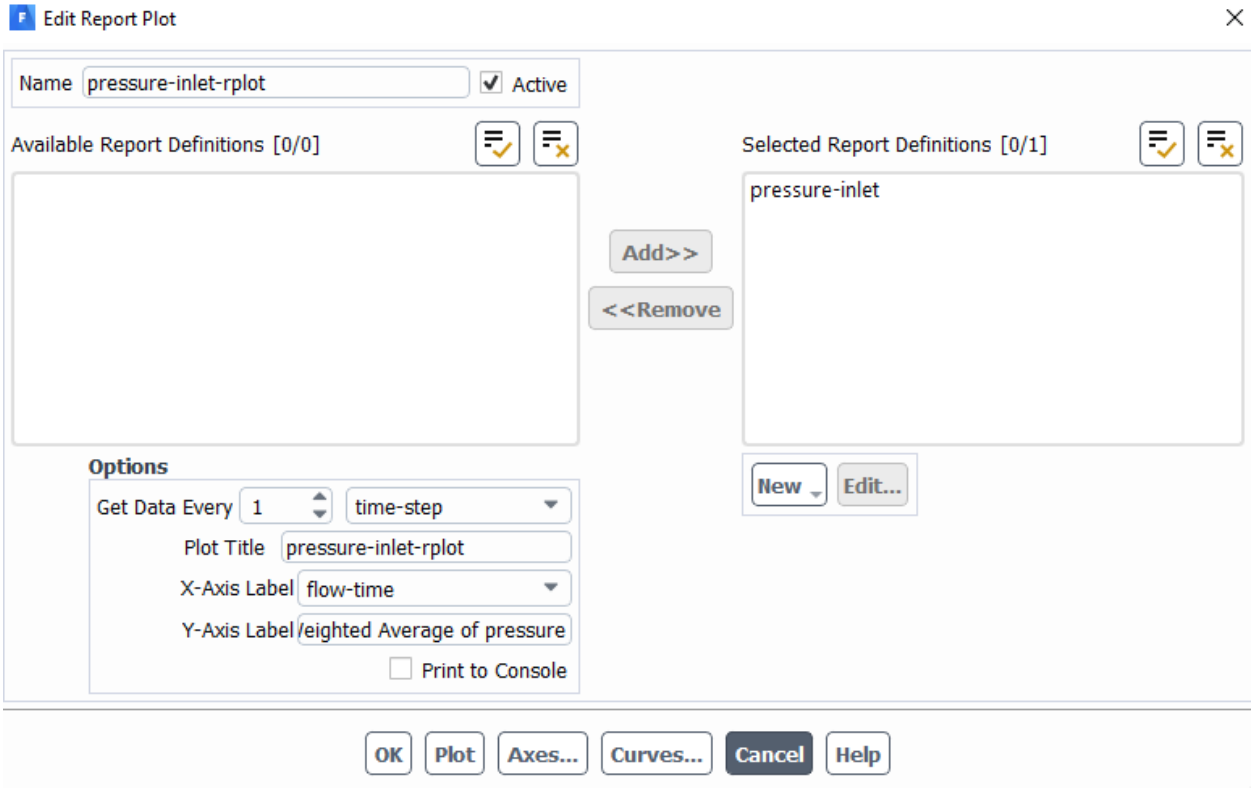

Figure 37: Solution Initialization Setup

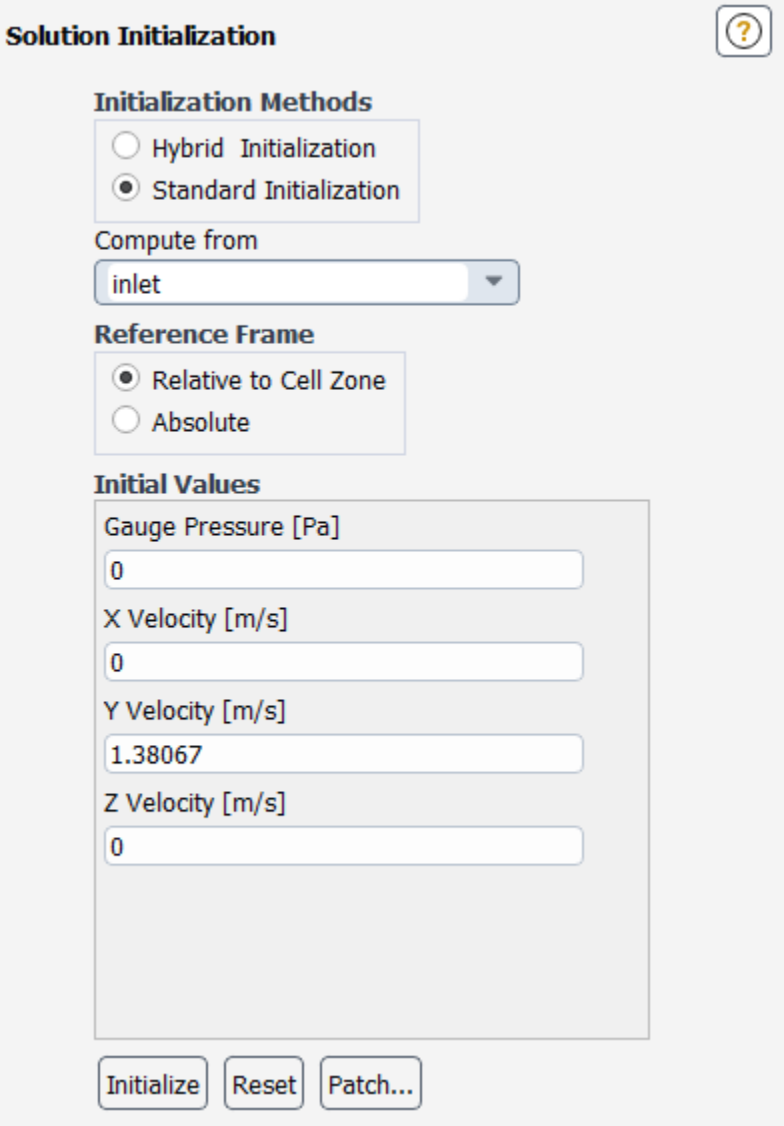

Figure 38: Setting Calculation Parameters

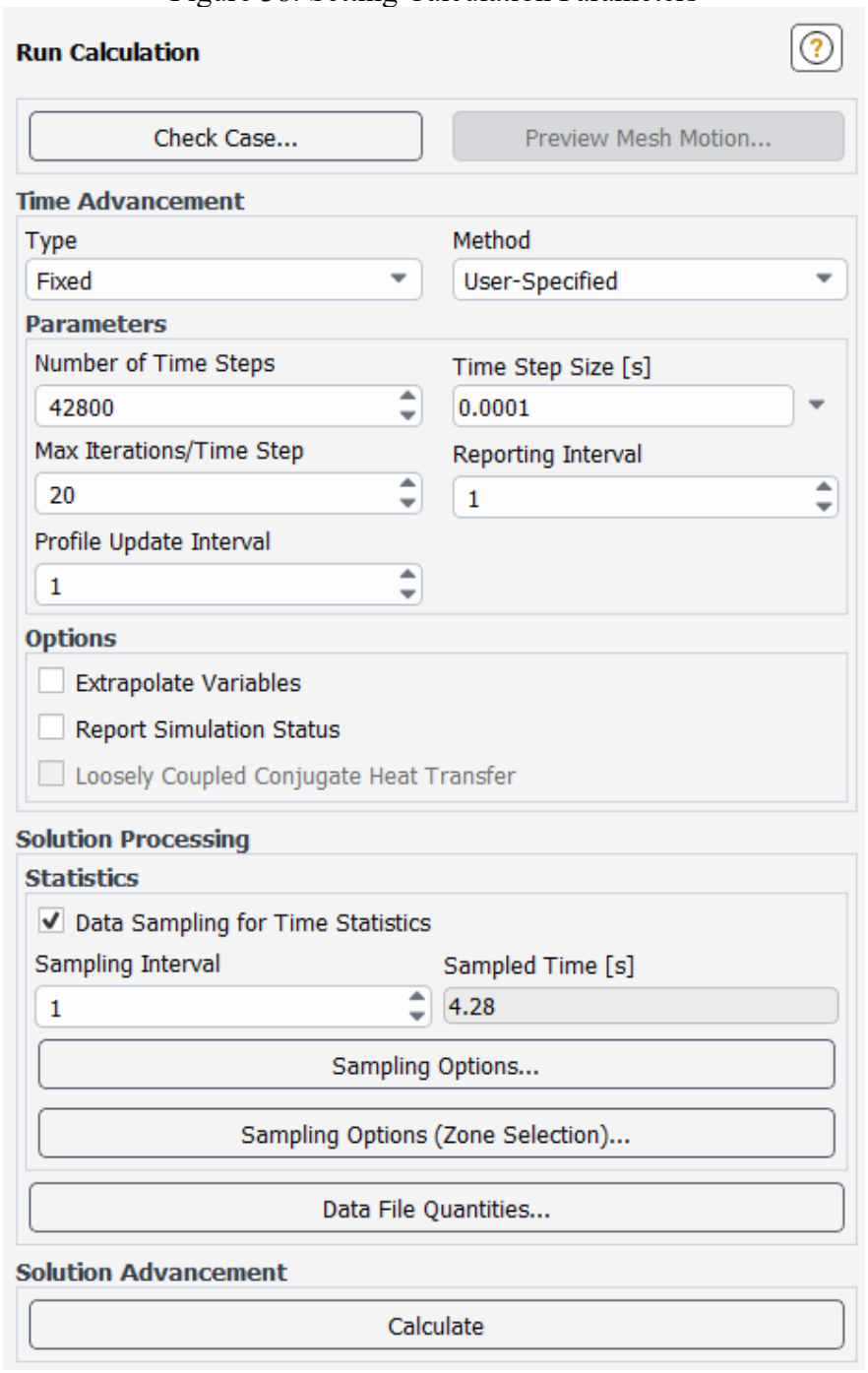

REFERENCES

Ahmad, N., Salama, D., & Al-Haggar, M. (2021). MRI CSF flowmetry in evaluation of different neurological diseases. *Egyptian Journal of Radiology, 52*(53), 1-10.

Bergen, M. P. (1982). Some histological aspects of the structure of the connective tissue system and its relationships with the blood vessels in the human orbit. *Acta Morphologica Neerlando-Scandinavica, 20*(4), 293-308.

Bloomfield, I. G., Johnston, I. H., & Bilston, L. E. (1998). Effects of proteins, blood cells and glucose on the viscosity of cerebrospinal fluid. *Pediatric Neurosurgery, 28*(5), 246-251.

Bothwell, S. W., Janigro, D., & Patabendige, A. (2019). Cerebrospinal fluid dynamics and intracranial pressure elevation in neurological diseases. *Fluids & Barriers of the CNS, 16*(1).

Boye, D., Montali, M., Gruber, P., Remonda, L., Berberat, J., Miller, N. R., . . . Killer, H. E. (2018). Flow dynamics of cerebrospinal fluid between the intracranial cavity and the subarachnoid space of the optic nerve measured with a diffusion magnetic resonance imaging sequence in patients with normal tension glaucoma. *Clinical & Experimental Ophthalmology, 46*(5), 511-518.

Damor, P., & Vatukiya, S. (2021). Ultrasound assessment of optic nerve sheath diameter for evaluation of elevated intracranial pressure in patient with head trauma: A comparative study with CT head. *International Journal of Radiology and Diagnostic Imaging, 4*(2), 1-4.

Downs, J. C., & Girkin, C. A. (2017). Lamina cribrosa in glaucoma. *Current Opinion in Ophthalmology, 28*(2), 113-119.

Dunn, L. T. (2002). Raised intracranial pressure. *Journal of Neurology, Neurosurgery, and Psychiatry, 73*(1), 23-27.

Feola, A. J., Coudrillier, B., Mulvihill, J., Geraldes, D. M., Vo, N. T., Albon, J., . . . Ethier, C. R. (2017). Deformation of the Lamina Cribrosa and Optic Nerve Due to Changes in Cerebrospinal Fluid Pressure. *Investigative Ophthamology & Visual Science, 58*(4), 2070-2078.

Hou, R., Zhang, Z., Yang, D., Wang, H., Chen, W., Li, Z., . . . Wang, N. (2016). Intracranial pressure (ICP) and optic nerve subarachnoid space pressure (ONSP) correlation in the optic nerve chamber: the Beijing Intracranial and Intraocular Pressure (iCOP) study. *Brain Research, 1635*, 201-208.

Ireland, A. C., & Carter, I. B. (2021). *Neuroanatomy, Optic Chiasm.* Treasure Island: StatPearls Publishing.

Johannesson, G., Eklund, A., & Linden, C. (2018). Intracranial and Intraocular Pressure at the Lamina Cribrosa: Gradient Effects. *Current Neurology and Neuroscience Reports, 18*(5), 25.

Jonas, J. B., Berenshtein, E., & Holbach, L. (2003). Anatomic relationship between lamina cribrosa, intraocular space, and cerebrospinal fluid space. *Investigative Ophthamology & Visual Science, 44*(12), 5189-5195.

Killer, H. E. (2013). Production and Circulation of Cerebrospinal Fluid With Respect to the Subarachnoid Space of the Optic Nerve. *Journal of Glaucoma, 22*(5), 8-10.

Killer, H. E., Flammer, J., Miller, N. R., Huber, A. R., Mironov, A., & Jaggi, G. (2007). Cerebrospinal fluid dynamics between the intracranial and the subarachnoid space of the optic nerve. Is it always bidirectional? *Brain: A Journal of Neurology, 130*(Pt 2), 514-520.

Killer, H. E., Jaggi, G. P., Flammer, J., Miller, N. R., & Huber, A. R. (2006). The optic nerve: a new window into cerebrospinal fluid composition? *Brain: A Journal of Neurology, 129*(4), 1027-1030.

Killer, H. E., Jaggi, G. P., Miller, N. R., Huber, A. R., Landolt, H., Mironov, A., . . . Remonda, L. (2011). Cerebrospinal fluid dynamics between the basal cisterns and the subarachnoid space of the optic nerve in patients with papilloedema. *The British Journal of Ophthamology, 95*(6), 822-827.

Killer, H. E., Laeng, H. R., Flammer, J., & Groscurth, P. (2003). Architecture of arachnoid trabeculae, pillars, and septa in the subarachnoid space of the human optic nerve: anatomy and clinical considerations. *The British Journal of Ophthamology, 86*(6), 777-781.

Killer, H. E., Miller, N. R., Flammer, J., Meyer, P., Weinreb, R. N., Remonda, L., & Jaggi, G. P. (2012). Cerebrospinal fluid exchange in the optic nerve in normal-tension glaucoma. *British Journal of Ophthalmology, 96*(4), 544-548.

Korbecki, A., Zimny, A., Podgorski, P., Sasiadek, M., & Bladowska, J. (2019). Imaging of cerebrospinal fluid flow: fundamentals, techniques, and clinical applications of phase-contrast magnetic resonance imaging. *Polish Journal of Radiology, 84*, 240-250.

Li, Z., Yang, Y., Lu, Y., Liu, D., Xu, E., Jia, J., . . . Wang, N. (2012). Intraocular pressure vs intracranial pressure in disease conditions: a prospective cohort study (Beijing iCOP study). *BMC Neurology, 12*(66), 1-4.

Lindstrom, E. K., Ringstad, G., Mardal, K. A., & Eide, P. K. (2018). Cerebrospinal fluid volumetric net flow rate and direction in idiopathic normal pressure hydrocephalus. *NeuroImage, 20*, 731-741.

Liu, D., & Michon, J. (1995). Measurement of the subarachnoid pressure of the optic nerve in human subjects. *American Journal of Ophthamology, 119*(1), 81-85.

Liu, H., Yang, D., Ma, T., Shi, W., Zhu, Q., Kang, J., & Wang, N. (2018). Measurement and Associations of the Optic Nerve Subarachnoid Space in Normal Tension and Primary Open-Angle Glaucoma. *American Journal of Ophthalmology, 186*, 128-137.

Morgan, W. H., Balaratnasingam, C., Lind, C. R., Colley, S., Kang, M. H., House, P. H., & Yu, D. Y. (2016). Cerebrospinal fluid pressure and the eye. *The British Journal of Ophthamology, 100*(1), 71-77.

Morgan, W. H., Lind, C. R., Kain, S., Fatehee, N., Bala, A., & Yu, D. Y. (2012). Retinal vein pulsation is in phase with intracranial pressure and not intraocular pressure. *Ophthamology & Visual Science, 53*(8), 4676-4681.

Nabeta, H. W., Bahr, N. C., Rhein, J., Fossland, N., Kiragga, A. N., Meya, D. B., . . . Boulware, D. R. (2014). Accuracy of noninvasive intraocular pressure or optic nerve sheath diameter measurements for predicting elevated intracranial pressure in cryptococcal meningitis. *Open Forum Infectious Diseases, 1*(3).

Nag, D. S., Swain, A., & Kant, S. (2019). Intracranial pressure monitoring: Gold standard and recent innovations. *World Journal of Clinical Cases, 7*(13), 1535-1553.

Ohno-Matsui, K., Akiba, M., Moriyama, M., Ishibashi, T., Tokoro, T., & Spaide, R. (2011). Imaging Retrobulbar Subarachnoid Space around Optic Nerve by Swept-Source Optical Coherence Tomography in Eyes with Pathologic Myopia. *52*(13), 9644-9650.

Padayachy, L., Brekken, R., Fieggen, G., & Selbekk, T. (2019). Noninvasive Transorbital Assessment of the Optic Nerve Sheath in Children: Relationship Between Optic Nerve Sheath Diameter, Deformability Index, and Intracranial Pressure. *Operative Neurosurgery, 16*(6), 726-733.

Shafique, S., & Rayi, A. (2021). *Anatomy, Head and Neck, Subarachnoid Space.* Treasure Island: StatPearls Publishing.

Sharp, K. M., Carare, R. O., & Martin, B. A. (2019). Dispersion in porous media in oscillatory flow between flat plates: applications to intrathecal, periarterial and paraarterial solute transport in the central nervous system. *Fluids and Barriers of the CNS, 16*(1), 13.

Sokolowski, W., Barszcz, K., Kupczynska, M., Czubai, N., Skibniewski, M., & Purzyc, H. (2018). Lymphatic drainage of cerebrospinal fluid in mammals - are arachnoid granulations the main route of cerebrospinal fluid outflow? *Biologia, 73*(6), 563-568.

Stead, G., Cresswell, F., Jjunju, S., Oanh, P., Thwaites, G., & Donovan, J. (2021). The role of optic nerve sheath diameter ultrasound in brain infection. *eNeurologicalSci, 23*(100330), 1-6.

Telano, L. N., & Baker, S. (2021). *Physiology, Cerebral Spinal Fluid.* Treasure Island: StatPearls Publishing.

Visual Loss: Disorders of the Chiasm. (2019, December 26). Retrieved from Ento Key: https://entokey.com/visual-loss-disorders-of-the-chiasm/

Vital Signs (Body Temperature, Pulse Rate, Respiration Rate, Blood Pressure). (2021). Retrieved from Johns Hopkins Medicine: https://www.hopkinsmedicine.org/health/conditions-and-diseases/vital-signs-body-temperature-pulse-rate-respiration-rate-blood-pressure

Vurgese, S., Panda-Jonas, S., & Jonas, J. B. (2012). Scleral thickness in human eyes. *PLoS One, 90*(2), 277-284.

Wilson, M. H. (2016). Monro-Kellie 2.0: The dynamic vascular and venous pathophysiological components of intracranial pressure. *Journal of Cerebral Blood Flow & Metabolism, 36*(8), 1338-1350.

Yatsushiro, S., Sunohara, S., Atsumi, H., Matsumae, M., & Kuroda, K. (2018, January 26). *Visualization and characterization of cerebrospinal fluid motion based on magnetic resonance imaging. In Hydrocephalus: Water on the Brain.* Retrieved from IntechOpen: https://www.intechopen.com/chapters/58993

VITA

Vincent Kent was born and raised in Independence, Missouri. He attended William Chrisman High School and graduated May 2016 after completing his coursework. After receiving his high school diploma, he entered the University of Missouri-Kansas City in the fall of 2016. From February 2018 to June 2020, he was employed by Northrop Grumman as a mechanical engineering intern. He received his Bachelor of Science in Mechanical Engineering from the University of Missouri-Kansas City in May 2020. Upon completing his undergraduate studies, he was employed as an Associate Mechanical Engineer for Northrop Grumman between June and October of 2020. In addition to his employment he entered the University of Missouri-Kansas City for graduate studies in August 2020. Then in October 2020, he began employment as a Project Engineer for Olin Winchester. While employed, he completed his Masters of Science in Mechanical Engineering from the University of Missouri-Kansas City in December 2021.